

# 1 Quantification of Delayed Recharge by Soil Surface and Riverbed 2 Infiltration in a Deep Groundwater Depression Zone in the North 3 China Plain

4 Shenghao Xu<sup>1</sup>, Yonggen Zhang<sup>2\*</sup>, Xinwang Li<sup>3</sup>, Jianzhu Li<sup>1</sup>, Wenhao Shi<sup>2</sup>, Shaowei Lian<sup>4</sup>, Lei Li<sup>5</sup>, Lutz  
5 Weihermüller<sup>6</sup>, Marcel Schaap<sup>7</sup>

6 <sup>1</sup>State Key Laboratory of Hydraulic Engineering Intelligent Construction and Operation, Tianjin University, Tianjin 300350,  
7 China

8 <sup>2</sup>Institute of Surface-Earth System Science, School of Earth System Science, Tianjin University, Tianjin 300072, China

9 <sup>3</sup>Hebei Institute of Water Science (Hebei province dam safety technology center, Hebei province levee sluice technology  
10 center), Shijiazhuang 050051, China

11 <sup>4</sup>Hebei Provincial Hydrologic Survey and Research Center, Shijiazhuang 050051, China

12 <sup>5</sup>Ninth Geological Brigade of Hebei Bureau of Geology and Mineral Resources, Xingtai 054000, China

13 <sup>6</sup>Agrosphere Institute IBG-3, Forschungszentrum Jülich GmbH, Jülich 52428, Germany

14 <sup>7</sup>Department of Environmental Science, University of Arizona, Tucson 85721, USA

15 *Correspondence to:* Yonggen Zhang ([ygzhang@tju.edu.cn](mailto:ygzhang@tju.edu.cn))

16 **Abstract.** Agriculture on the North China Plain (NCP), home to over 300 million people, heavily relies on groundwater  
17 extraction to feed its irrigation systems. This has created a large groundwater depression zone up to 80 m deep, severely  
18 limiting sustainable groundwater extraction and crop production. Effective recharge is essential to restore this depleted zone  
19 and secure future sustainability. Few studies have quantified recharge delays and efficiencies in deep vadose zones with  
20 complex lithology. Here we simulated infiltration times and percolation velocities in the Ningbailong groundwater depression  
21 zone, a typical overexploited site in the NCP using HYDRUS-1D with measured borehole lithology and hydro-meteorological  
22 data. Two infiltration modes, precipitation-fed soil infiltration and riverbed infiltration, were considered. Spatial distributions  
23 of infiltration times and percolation velocities were obtained, and recharge efficiencies were compared between these two  
24 infiltration modes. Results showed that times for precipitation-fed recharge averaged 446 days and varied with lithology and  
25 thickness, from 10 days in western Taihang foothills (dominated by coarse sands) to 1,395 days in central/eastern plains (finer  
26 clays and loams). Riverbed recharge was markedly faster, averaging 91 days, indicating higher infiltration efficiency than  
27 precipitation under equivalent lithological conditions. Regression equations were derived to predict percolation velocities using  
28 vadose zone thickness, sand fraction, and clay fraction as key predictors. These findings elucidate how vadose zone thickness  
29 and lithology amplify recharge lags and control recharge efficiency. They also highlight the potential for managed aquifer  
30 recharge strategies, such as constructing infiltration basins for flood capture, offering strategies to reduce groundwater over-  
31 exploitation in similar depression zones.

## 32 **1 Introduction**

33 Groundwater recharge is a critical process in the hydrological cycle and a fundamental component in groundwater resources.  
34 The depletion of aquifers, driven by groundwater over-exploitation, has become a pressing global concern (Wang et al., 2010;  
35 Kuang et al., 2024; Karandish et al., 2025), resulting in geological hazards such as land subsidence, seawater intrusion, and  
36 wells running dry (Scanlon et al., 2023; Shirzaei et al., 2021; Jasechko and Perrone, 2021). Groundwater recharge primarily  
37 occurs through precipitation-fed soil surface infiltration and riverbed infiltration. In the North China Plain (NCP), which feeds  
38 300 million people, approximately 70% of the shallow groundwater recharge comes from precipitation-fed infiltration through  
39 soils (Liu et al., 2022). Quantification of the efficiency of this process in relation to riverbed infiltration as controlled by  
40 variability in vadose zone lithologies is fundamental to sustainable utilization and scientific management of depleted  
41 groundwater zones.

42 Extensive research has explored the principles of infiltration in the vadose zone based on the theory of unsaturated soil water  
43 movement. This theory governs how water infiltrates through partially saturated porous media under the influences of gravity  
44 and matric potential gradients (Assouline, 2013; Vereecken et al., 2019; Christine and Gerhard, 2022; Schübl et al., 2023; Gao  
45 et al., 2024). Consequently, these studies highlight the critical role that heterogeneities in soil lithology (soil texture), structure,  
46 and vadose zone depth can play in regulating infiltration rates, lag times, and overall recharge efficiency, particularly in  
47 overexploitation regions (Szabó et al., 2019; Turkeltaub et al., 2015).

48 Among various surface inputs, precipitation-fed infiltration emerges as the primary driver of vadose zone and groundwater  
49 recharge, directly linking atmospheric inputs to subsurface hydrology through vertical percolation. For instance, Dafny and  
50 Šimůnek (2016) investigated layered loess deposits in Israel's coastal plain. They calibrated van Genuchten parameters using  
51 a HYDRUS-2D/3D model informed by infiltration tests, confirming that saturated conductivities vary significantly across  
52 different soil lithologies. Employing HYDRUS-1D with 25-year meteorological data, they further demonstrated that vegetation  
53 reduces recharge through enhanced transpiration. Moreover, sediment layering caused lag times of 2.5-20 years for wetting  
54 fronts to reach a 22 m depth, emphasizing lithological control on infiltration efficiency in arid areas. Jie et al. (2022) quantified  
55 vadose zone thickness impacts on delayed recharge in Jingdian Irrigation District in Northwest China using HYDRUS-1D.  
56 Their simulations revealed a linear increase in lag times (up to 5,000 days for depths >8 m). Consequently, overall recharge  
57 rates were significantly reduced as the vadose zone thickness increased.

58 Extending this perspective to global scales, Moeck et al. (2024) assessed groundwater recharge responses to monthly-decadal  
59 infiltration variability using an analytical solution of the Richards equation. They found that vadose zones dampen short-term  
60 fluctuations globally, with lags exceeding years in arid regions and transient recharge driven by multi-annual cycles such as  
61 ENSO. As depth increases, the correlation between infiltration and recharge weakens. More recently, Yin et al. (2025) utilized  
62 GRACE data and wavelet transforms to analyze precipitation-fed recharge from the Heilongjiang Basin in China. They  
63 identified dominant 1-2 year cycles with lags of 2-6 months in plain areas. These hydrological responses are heavily modulated  
64 by topography and soil type, highlighting an accelerated dynamic under climate change.

65 Riverbed infiltration is another important pathway through which surface water recharges groundwater. Empirical studies have  
66 demonstrated that this process can also have significant effects on groundwater recharge (Dillon et al., 2019, Niswonger et al.,  
67 2005). In regions with low precipitation and high actual evapotranspiration, or in areas with concentrated water inputs from  
68 intermittent streams, groundwater recharge is dominated by riverbed infiltration, while precipitation-driven infiltration  
69 minimally contributes to groundwater recharge (Bierkens et al., 2021). The key factors influencing riverbed infiltration include  
70 the material composition of the riverbed, the hydraulic gradient between the river and groundwater, as well as aquifer  
71 characteristics (Shanafield et al., 2020). However, due to the lack of direct methods for monitoring the riverbed infiltration, it  
72 is typically analyzed through continuous observations of the river water levels, soil water content in the infiltration zone, and  
73 groundwater levels. Ruehl et al. (2006) utilized hydrological station data and tracer tests to quantify river leakage rates and  
74 assess the reliability of conceptual models and quantitative approaches for studying river leakage processes. Xi et al. (2015)  
75 investigated the saturated permeability coefficient of the riverbed in the lower reaches of the Heihe River Basin, Northwest  
76 China by using the Guelph Permeameter and laboratory analysis methods and analyzed the characteristics of riverbed  
77 infiltration and its spatial distribution patterns. They found that the saturated permeability coefficient exhibited a moderate  
78 degree of spatial heterogeneity, with the riverbed material composition, initial soil water content and bulk density having  
79 primary impacts on riverbed infiltration. Secondary effects controlling riverbed infiltration included topographic factors such  
80 as riverbed width, altitude, hydraulic gradient, and riverbed curvature. Di Ciacca et al. (2024) proposed a model simplification  
81 framework that transitions from complex 3D integrated hydrological models to simpler 1D analytical conductance models for  
82 simulating groundwater recharge in perched gravel-bed rivers, with application to the Selwyn River in New Zealand. They  
83 emphasized the critical influence of riverbed sediment storage and groundwater levels in shallow aquifer on time-variable  
84 infiltration rates and recharge volumes under seasonal river conditions.

85 In general, research on groundwater recharge has primarily focused on vertical infiltration into the vadose zone. Widely used  
86 methods for evaluating infiltration recharge volumes include physical methods (e.g., Racz et al., 2012; Ganot et al., 2017),  
87 tracer methods (e.g., Wang et al., 2024), and mathematical models (e.g., Vereecken et al. 2019; Šimůnek et al., 2012; Arnold  
88 et al., 2012). A comprehensive overview of mathematical models for infiltration processes was provided by Vereecken et al.  
89 (2019). These models range from empirical approaches, such as the Kostikov equation (1932) and Horton equation (1941) to  
90 analytical solutions such as the Green-Ampt (1911) and Philip (1957) models. Importantly, they emphasized the Richards  
91 equation as the fundamental framework for unsaturated flow. This framework incorporates essential soil hydraulic properties  
92 such as the water retention curve  $\theta(h)$  (e.g., Brooks and Corey, 1964; van Genuchten, 1980) and hydraulic conductivity  $K(h)$ .  
93 For complex, real-world infiltration problems (e.g., layered soil profiles, variable initial saturation, time-variable rainfall, and  
94 limited ponding), quantitative analysis is typically achieved through numerical solutions of the Richards equation.

95 Leveraging computational advances over the past decades, several software codes have been developed to simulate vadose  
96 zone infiltration and groundwater recharge dynamics by numerically solving the Richards equation and related processes.  
97 Well-known methods include HYDRUS (Šimůnek et al., 2012, 2016, 2024), SWAP (Van Dam et al. 2008; Kroes and Supit  
98 2011), and SWMS (Li et al., 2019). Among these, HYDRUS-1D is a one-dimensional soil water model that comprehensively

99 accounts for precipitation, vegetation water uptake, evaporation, soil water movement, and groundwater table fluctuations  
100 (Assefa and Woodbury, 2013; Stafford et al., 2022; Dadgar et al., 2018).

101 The practical utility of HYDRUS-1D has been demonstrated across various spatial scales and environmental conditions. For  
102 instance, Assefa and Woodbury (2013) integrated field observations with HYDRUS-1D to model transient, spatially varied  
103 groundwater recharge in North Okanagan, Canada. Coupled with ArcGIS, the model produced recharge maps for the Deep  
104 Creek watershed, estimating average recharge at  $77.8 \pm 50.8$  mm year<sup>-1</sup> over 25 years, with significant spatiotemporal  
105 variability. More recently, Wolf et al. (2022) advanced the understanding of recharge mechanisms in thick vadose zones (14-  
106 38 m) under varying land use/land cover and climate conditions. By calibrating HYDRUS-1D models using monitoring data  
107 from the High Plains aquifer, they suggested that land use/land cover is a major controlling factor. In addition, they found that  
108 irrigated sites exhibited relatively short lag times of 20-24 months, contrasting sharply with extended lags of 5-31 years at  
109 rangeland sites. These studies show that HYDRUS-1D is a valuable tool for quantifying recharge rates and time-delay of deep-  
110 vadose zone groundwater under a wide spectrum of environmental conditions.

111 The North China Plain (NCP), one of China's three major plains and home to over 300 million people in one of the world's  
112 most densely populated regions, is an important area for agricultural production, with groundwater serving as the primary  
113 water resource for irrigation (Long et al., 2025). Since the late 1970s, groundwater extraction has intensified in this area,  
114 resulting in long term over-exploitation. This has led to the formation of large-scale groundwater depression, making the NCP  
115 one of the largest groundwater depression zones in the world (Chen et al., 2020). For instance, in the Ningbailong and  
116 Gaolisurao regions, where groundwater levels continue to decline, agricultural irrigation became unsustainable (Liu et al.,  
117 2022). The substantial decline in groundwater levels has resulted in the formation of a thick vadose zone, affecting water  
118 infiltration at the soil surface and groundwater recharge at depth. A holistic understanding of soil water movement in these  
119 deeper vadose zones is therefore crucial for evaluating recharge mechanisms and developing effective strategies for sustainable  
120 groundwater management. Based on field experiments and observations of actual evapotranspiration measured by eddy  
121 covariance, Min et al. (2015) used HYDRUS-1D to investigate the vertical infiltration and infiltration characteristics of a thick  
122 vadose zone in irrigated farmland in the foothill region of the Taihang Mountains located in the North China Plain. Huo et al.  
123 (2014) applied a one-dimensional variably saturated flow model to examine the influence of increasing vadose zone thickness  
124 on vertical groundwater recharge in the NCP, and the results showed that as the vadose zone thickens, the magnitude and  
125 timing of recharge are significantly altered, with delayed infiltration responses and reduced recharge reaching the water table.  
126 Recently, Zhou et al. (2023) quantitatively assessed the sustainability of groundwater in the NCP based on monitoring  
127 observations from 556 wells during the period of 2005-2018, using indices such as reliability, vulnerability, and sustainability.  
128 They highlighted the weak recovery capacity of the groundwater and identified non-climatic factors as the dominant drivers  
129 of depletion in the NCP, emphasizing the profound implications for sustainable water resource management in the region.

130 Despite the fact that there have been substantial advances in the quantification of precipitation-fed groundwater recharge, few  
131 efforts have addressed the challenges in areas with deepening groundwater levels and complex vadose zone lithology. In such  
132 areas, groundwater recharge takes much longer due to delayed water percolation through thick variable unsaturated zones, yet

133 few studies have explicitly quantified the resulting lag times and percolation velocities. More importantly, existing studies  
134 have analysed precipitation infiltration and riverbed infiltration independently. Consequently, systematic comparison of their  
135 recharge efficiencies under identical vadose zone conditions remain scarce, particularly in terms of infiltration times and rates  
136 across heterogeneous vadose zones. As one of the world's largest groundwater depression zones, the NCP serves as a typical  
137 region for studying infiltration dynamics under intensive overexploitation, where incorporating actual vadose zone borehole  
138 data and hydrogeological conditions into quantitative analyses of infiltration times and average percolation velocities can  
139 elucidate recharge efficiencies of different sources, including precipitation and riverbed infiltration. This approach also offers  
140 insights into spatially heterogeneous groundwater replenishment dynamics across various regions.

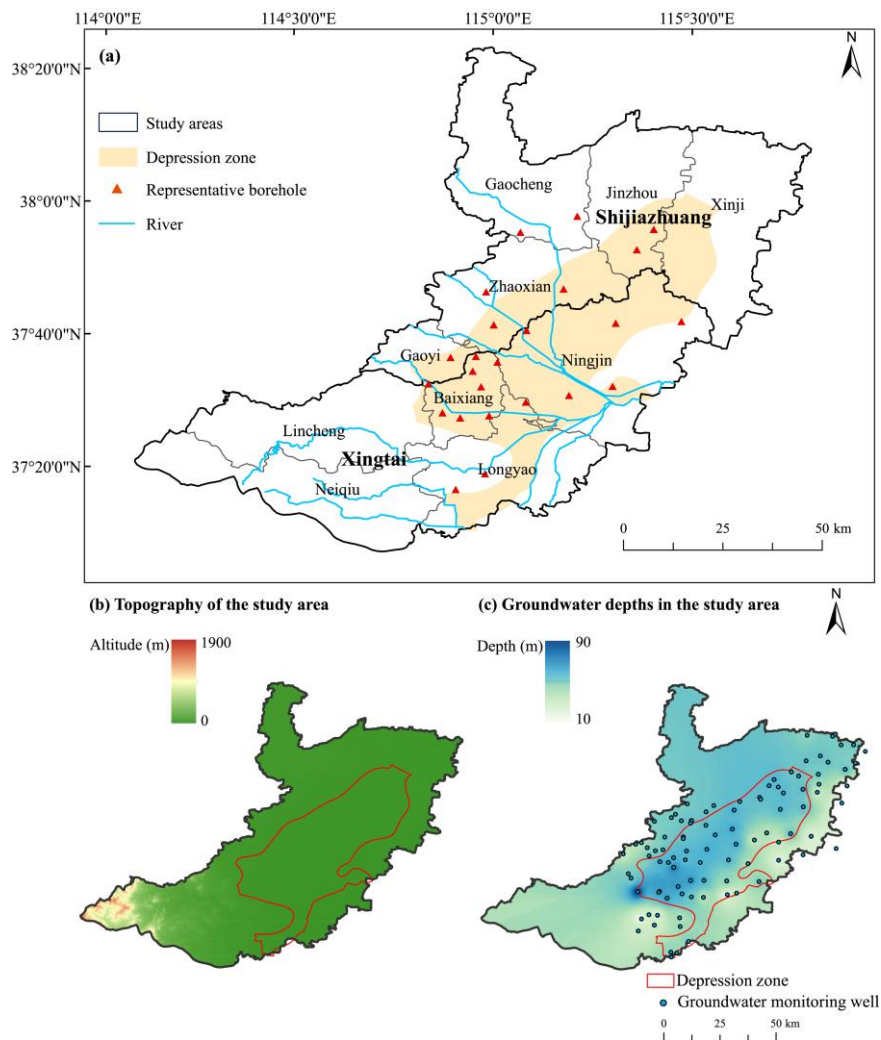
141 The main objectives of this paper are to: (1) quantitatively assess the groundwater infiltration times and percolation velocities  
142 under two recharge regimes (i.e., precipitation-fed infiltration and riverbed infiltration), using measured borehole lithological  
143 data and hydrometeorological observations from the Ningbailong groundwater depression zone; (2) analyze the spatial  
144 distribution of infiltration times and percolation velocities across the region, accounting for vadose zone heterogeneity  
145 influenced by thickness and lithology; and (3) compare the recharge efficiencies of precipitation and riverbed infiltration  
146 sources under equivalent vadose zone conditions, provide the empirical regression equation for the percolation velocities under  
147 the two recharge regimes, and propose appropriate groundwater recharge methods at the corresponding locations based on the  
148 comparison results. The results of this study are anticipated to provide a basis for assessing groundwater over-exploitation and  
149 developing management measures in similar depression zones.

## 150 **2 Materials and methods**

### 151 **2.1 Study area**

152 The Ningbailong shallow groundwater depression zone is located in Xingtai City, Hebei Province, China, as shown in Figure  
153 1, within one of the main grain-producing regions in the NCP, where a double-cropping rotation of winter wheat and summer  
154 maize is the dominant cropping system. The area of the depression zone is 2,092 km<sup>2</sup>, with the main river within it covering  
155 approximately 7.2 km<sup>2</sup>, accounting for 0.35% of the total area. This area spans the western part of Ningjin County, most of  
156 Baixiang County, and the northern to central part of Longyao County and it is expanding to the southern part of Shijiazhuang  
157 city. The region lies at the junction of the Taihang Mountains and the North China Plain, characterized by a temperate semi-  
158 humid to semi-arid continental monsoon climate, with an annual average precipitation of 540 mm and an annual average  
159 potential evaporation of 1,600 mm. The study area borders the Taihang Mountains to the southwest, adjoins Shijiazhuang to  
160 the northwest, connects with Hengshui to the northeast, and is adjacent to Xingtai counties to the south and southeast. The  
161 topography of the Ningbailong depression zone slopes downward from west to east, with elevations decreasing from  
162 approximately 100 m in the western foothills to around 30 m in the eastern and northern regions, shown in Figure 1*b*. Due to  
163 its location near the Taihang Mountains, the surface of the western part of the depression zone has steeper slopes (1.5–2.5‰)  
164 than the northeastern part (0.5–1‰). Groundwater recharge in the Ningbailong depression zone primarily originates from

165 precipitation, irrigation, and lateral runoff, with precipitation contributing approximately 70% of total recharge. Recharge  
166 dynamics are modulated by vadose zone lithology, groundwater depth, topography, and vegetation, as evidenced by regional  
167 hydrogeological studies (Cao et al., 2016; Min et al., 2019). Notably, the foothill alluvial fans and eastern plain riverbed zones  
168 may have enhanced recharge due to their permeable sediments and close connection to surface water inputs. Since the late  
169 1970s, escalating agricultural water demand has intensified groundwater extraction in the region. Consequently, the  
170 Ningbailong groundwater depression zone has expanded in both depth and extent, rendering agricultural irrigation increasingly  
171 unsustainable due to persistent groundwater level declines and an uneconomical rise in extraction costs.



172  
173 **Figure 1: Study area of the Ningbailong groundwater depression zone in the North China Plain with (a) location of the Ningbailong**  
174 **groundwater depression zone, (b) topography, and (c) groundwater depth with groundwater monitoring wells as blue dots.**

175 **2.2 Data**

176 Hydrogeological data for the Ningbailong depression zone were sourced from the 9<sup>th</sup> Geological Brigade of the Hebei  
 177 Provincial Bureau of Geological and Mineral Exploration and Development, encompassing borehole logs, water supply wells,  
 178 pumping test results, geophysical prospecting data, and groundwater level contour maps. From January 1, 2018 to December  
 179 31, 2023, dynamic groundwater level monitoring has provided continuous data to characterize temporal variability in the  
 180 depression zone. Vadose zone profile data, including lithological type, soil water content, and vadose zone thickness, were  
 181 collected from multiple sampling sites across the region to assess vadose zone heterogeneity. The lithology of the study area  
 182 was analyzed and conceptualized using borehole logs for 24 groundwater wells (see Table 1). In Table 1, the “Infiltration  
 183 Mode” column uses “P” or “R” to respectively indicate that the well is currently receiving precipitation-fed or riverbed  
 184 infiltration, and “Depth” represents the vadose zone thickness.

185 The meteorological and hydrological data for the study area were provided by the Xingtai Hydrological Survey and Research  
 186 Center of Hebei Province. These data include daily precipitation, potential evapotranspiration, river water level records from  
 187 the local precipitation stations and hydrological stations since 2014. These datasets served as driving data for simulating the  
 188 two infiltration scenarios (precipitation-fed soil infiltration and riverbed recharge).

189 **Table 1: Representative borehole data in the Ningbailong groundwater depression zone in the North China Plain. The infiltration**  
 190 **mode column specifies the recharge mode for each borehole, where “P” represents precipitation-fed infiltration and “R” represents**  
 191 **riverbed infiltration.**

Borehole Name	Infiltration Mode	Location	Depth(cm)	Latitude(° )	Longitude(° )
Bai 1	P	Baixiang, Xingtai	4960	37.6123	114.7186
Bai 10	P	Baixiang, Xingtai	6720	37.5434	114.7301
Bai 11	R	Baixiang, Xingtai	5080	37.4845	114.6427
Bai 12	P	Baixiang, Xingtai	8080	37.5787	114.7110
Bai 18	P	Baixiang, Xingtai	6150	37.4729	114.6828
Xisucun	P	Baixiang, Xingtai	4060	37.5992	114.7671
Xiaonanyangcun	P	Baixiang, Xingtai	5750	37.4777	114.7484
Hancun	R	Baixiang, Xingtai	5120	37.5501	114.6109
Ning 17	P	Ningjin, Xingtai	5960	37.6709	114.8331
San 62	P	Ningjin, Xingtai	5170	37.6913	115.1836
Ning 18	P	Ningjin, Xingtai	4600	37.5444	115.0280
Ning 20	P	Ningjin, Xingtai	3150	37.6873	115.0348
ZK 1	P	Ningjin, Xingtai	4200	37.5238	114.9289
Guoce 510	R	Longyao, Xingtai	3620	37.3460	114.7390
Long 8	P	Longyao, Xingtai	5960	37.5086	114.8314
Long 12	P	Longyao, Xingtai	2130	37.3108	114.6725
Gao 1	P	Gaoyi, Shijiazhuang	5640	37.6100	114.6611
Zhao 1	P	Zhaoxian, Shijiazhuang	5290	37.6836	114.7588
Zhao 2	P	Zhaoxian, Shijiazhuang	5350	37.7585	114.7415

Borehole Name	Infiltration Mode	Location	Depth(cm)	Latitude(° )	Longitude(° )
CK 18	P	Zhaoxian, Shijiazhuang	6560	37.7648	114.9168
CK 21	P	Jinzhou, shijiazhuang	5700	37.9000	115.1211
CK 22	P	Jinzhou, shijiazhuang	5410	37.8541	115.0827
CK 3	P	Gaocheng, shijiazhuang	4860	37.9298	114.9478
CK 10	P	Gaocheng, shijiazhuang	4660	37.8936	114.8191

## 192 2.3 Simulation setup

193 This study employed the HYDRUS-1D model (Šimůnek et al., 2012, 2024) to simulate one-dimensional soil water movement  
194 in the unsaturated zone by numerically solving the Richards equation. Widely applied in groundwater recharge investigations,  
195 HYDRUS-1D effectively captures soil water dynamics under varying recharge scenarios in the vadose zone.

196 This study considered only one-dimensional vertical flow, neglecting horizontal overland flow and lateral movement of soil  
197 water in the vadose zone. The ground surface is taken as the origin of the coordinate system, with the positive direction of the  
198 z-axis pointing downward. The Richards equation for one-dimensional saturated-unsaturated zone soil water movement is  
199 given by:

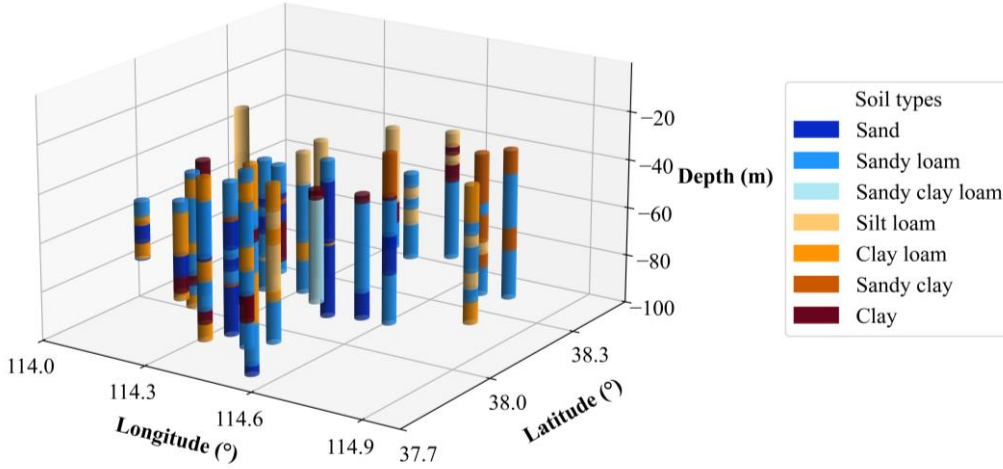
$$200 \quad \frac{\partial \theta}{\partial t} = \frac{\partial}{\partial z} \left[ K(\theta) \left( \frac{\partial h}{\partial z} \right) + K(\theta) \right] - S(z, t) \quad (1)$$

201 where  $\theta$  is the volumetric soil water content ( $\text{cm}^3 \text{ cm}^{-3}$ ),  $t$  represents time (d),  $z$  represents the soil depth (cm),  $K(\theta)$  indicates  
202 the unsaturated hydraulic conductivity ( $\text{cm d}^{-1}$ ) with respect to water content,  $h$  represents the pressure head (cm), which is  
203  $h \geq 0$  in the saturated zone and  $h < 0$  in the unsaturated zone, and  $S(z, t)$  is the root water uptake term ( $\text{d}^{-1}$ ), which is zero in bare  
204 areas.

205 In this study, the borehole data from Table 1 were selected to set up the HYDRUS-1D model for the individual locations. Two  
206 recharge source conditions, i.e., precipitation-fed and riverbed infiltration, were tested. The real-world recharge conditions are  
207 marked with a “P” or “R” in Table 1. However, we evaluated both infiltration boundary conditions for each borehole to a)  
208 maximize the number of results for each condition, and b) to evaluate whether a theoretical expansion of river-fed infiltration  
209 beyond the present 0.35% of the area (e.g., constructed infiltration basins) would be an effective way to enhance groundwater  
210 recharge in the area.

### 211 2.3.1 Vadose zone generalization

212 Based on hydrogeological survey data (Table 1), we parameterized the profiles for use with Hydrus-1D into seven simplified  
213 categories. For each borehole, soil profiles were stratified according to USDA soil classifications, as illustrated in Figure 2.  
214 These profiles were then discretized into 10 cm grid cells, with the total simulation depth set to the long-term average shallow  
215 groundwater elevation measured at the observation wells.



216  
 217 **Figure 2: USDA soil types and stratification for representative borehole in the study area.**

218 **2.3.2 Soil hydraulic parameters**

219 The soil hydraulic properties were described by the modified van Genuchten model (van Genuchten, 1980; Vogel et al., 2001).  
 220 The soil water retention characteristic  $\theta(h)$  and hydraulic conductivity  $K(\theta)$  are given by:

$$221 \quad \theta(h) = \begin{cases} \theta_r + \frac{\theta_m - \theta_r}{\left[1 + (\alpha h)^n\right]^m}, & h < h_s \\ \theta_s, & h \geq h_s \end{cases} \quad (2)$$

$$222 \quad K(h) = \begin{cases} K_s K_r(h), & h < h_s \\ K_s, & h \geq h_s \end{cases} \quad (3)$$

$$223 \quad K_r(S_e) = S_e' \left[ \frac{1 - F(S_e)}{1 - F(1)} \right]^2 \quad (4)$$

$$224 \quad F(S_e) = \left[ 1 - (S_e^*)^{1/m} \right]^m \quad (5)$$

$$225 \quad S_e(h) = \frac{\theta(h) - \theta_r}{\theta_s - \theta_r} \quad (6)$$

$$226 \quad S_e^* = \frac{\theta_s - \theta_r}{\theta_m - \theta_r} S_e \quad (7)$$

227 where  $\theta_r$  represents the residual soil water content ( $\text{cm}^3 \text{cm}^{-3}$ ),  $\theta_s$  indicates the saturated water content ( $\text{cm}^3 \text{cm}^{-3}$ ),  $\alpha$ ,  $n$ , and  $m$   
 228 are empirical parameters, whereby  $m$  can be related to  $n$  by  $m=1-1/n$ ,  $\theta_m$  represents the fictitious saturated water content slightly

229 larger than  $\theta_s$ , acting purely as a mathematical artifact to maintain the smooth analytical shape of the retention curve,  $h_s$  is the  
 230 air-entry pressure head (cm) used to improve numerical stability near saturation,  $K_s$  is the saturated hydraulic conductivity (cm  
 231  $\text{d}^{-1}$ ),  $K(h)$  represents the unsaturated hydraulic conductivity (cm  $\text{d}^{-1}$ ) at the pressure head  $h$ ,  $K_r$  represents the relative hydraulic  
 232 conductivity (-),  $l$  is the pore connectivity parameter usually assumed to be 0.5,  $S_e$  is the effective saturation (-), and  $Se^*$  is the  
 233 fictitious effective saturation (or scaled effective saturation), normalized by the fictitious saturated water content ( $\theta_m$ ). Based  
 234 on borehole measurements and referring to relevant literature (Weihermüller et al., 2021), we adopted the improved  
 235 hierarchical pedotransfer function set (Rosetta3) developed by Zhang and Schaap (2017) to derive the van Genuchten  
 236 parameters and  $K_s$  as the soil hydraulic parameter values of the unsaturated zone. The resulting values are presented in Table  
 237 2.

238 **Table 2. Soil hydraulic parameters used for vadose zone modelling in this study.**

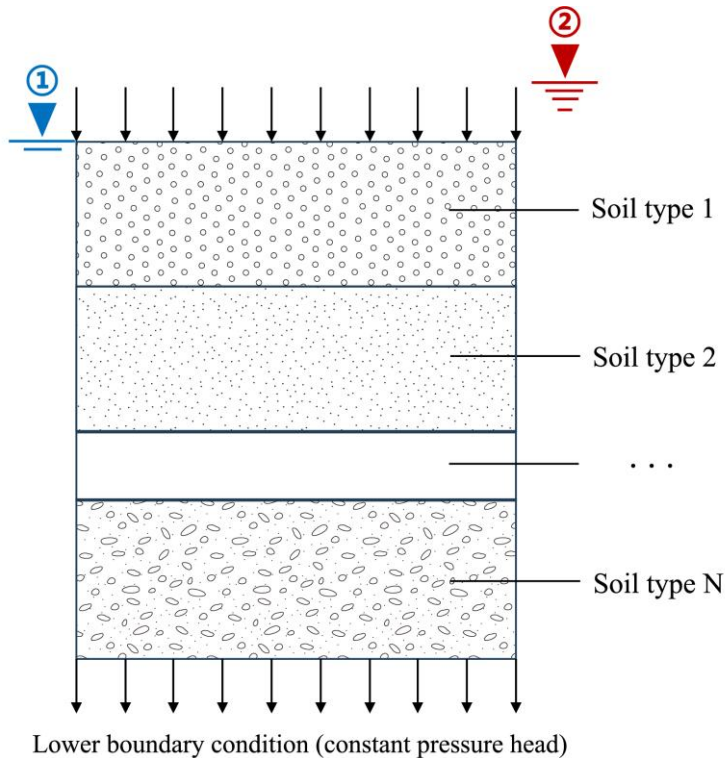
Soil type	$\theta_r$ ( $\text{cm}^3\text{cm}^{-3}$ )	$\theta_s$ ( $\text{cm}^3\text{cm}^{-3}$ )	$\alpha$ ( $\text{cm}^{-1}$ )	$n$ (-)	$K_s$ ( $\text{cm d}^{-1}$ )
sand	0.05	0.43	0.145	2.68	712.8
sandy loam	0.06	0.41	0.075	1.89	106.1
silt loam	0.07	0.45	0.020	1.41	10.8
sandy clay loam	0.10	0.39	0.059	1.48	31.4
clay loam	0.09	0.41	0.019	1.35	6.24
sandy clay	0.10	0.38	0.027	1.35	2.88
clay	0.07	0.38	0.008	1.31	4.8

### 239 2.3.3 Generalization of boundary conditions

240 The simulations were performed for a one-dimensional soil column under vegetated conditions, without accounting for lateral  
 241 flow, whereby the water movement was simulated under different recharge source types, i.e., precipitation or riverbed  
 242 infiltration. For the precipitation case, atmospheric boundary conditions were applied at the surface, allowing ponding at the  
 243 surface if precipitation exceeded soil infiltration capacity, with the minimum allowable surface pressure head ( $h_{\text{CritA}}$ ) set to  
 244 its default value of -100,000 cm. Excess ponded water was allowed to infiltrate at times where the soils allowed infiltration.  
 245 In contrast, the riverbed infiltration case employed variable pressure heads at the upper boundary to represent surface water  
 246 inputs. Since the groundwater levels fluctuate over time and depend on the volume of infiltration recharge from surface water,  
 247 incorporating a time-variable lower boundary would indeed provide a more realistic representation of the simulations. However,  
 248 due to the inherent uncertainties in future precipitation conditions and the primary focus of this study on the impact of vadose  
 249 zone characteristics on the infiltration process, a constant lower boundary was assumed for model simplification (Šimůnek et  
 250 al., 2016). Consequently, a constant pressure head condition was applied to the lower boundary in both scenarios, using the  
 251 average groundwater level from January 1, 2018 to December 31, 2023 as a fixed reference depth for calculating groundwater  
 252 infiltration times and velocity. Figure 3 illustrates the conceptualized vadose zone model setup for the boundary conditions  
 253 under the two recharge regimes. Within the study area, precipitation data were exclusively obtained from the Baixiang Rain  
 254 Gauge Station. Given the relatively small spatial extent of the study area and the availability of continuous, long-term historical

255 records at this station, the precipitation data from this station were utilized as the upper boundary input for all boreholes across  
256 the study area, covering the period from July 1, 2016 to July 31, 2023. The river water level data were obtained from the  
257 hydrological stations near the Bai 11, Hancun, and Guoce 510 boreholes during the flood season from July to August 2016,  
258 and then the same average water level data from these stations were applied to simulate the riverbed infiltration to all the  
259 boreholes that are not close to the river.

260 Data from the single rain gauge station and the averaged river stage time series were utilized as consistent inputs for the  
261 regional simulations due to the high continuity of their observational records. Furthermore, applying these uniform upper  
262 boundary conditions across the entire region effectively controlled for meteorological variations, thereby isolating and  
263 highlighting the primary influence of vadose zone characteristics on infiltration recharge.



Upper boundary condition under:

① precipitation infiltration (atmospheric boundary condition with surface layer);

264 ② riverbed infiltration (variable pressure head)

265 **Figure 3: Schematic diagram of soil column boundary generalization used in the HYDRUS-1D simulations for the simulation of**  
266 **precipitation infiltration and riverbed infiltration.**

### 267 2.3.4 Root water uptake

268 Root water uptake was simulated only for the precipitation-fed infiltration scenario, as vegetation is typically absent in  
269 riverbeds, rendering transpiration negligible in those cases. By omitting root water uptake, the model maximizes the water  
270 available for downward percolation, which contributes to an upper-bound estimation of infiltration volumes and percolation  
271 velocities for riverbed recharge. For root water uptake, the Feddes model (Wesseling and Feddes, 2006) was used, which is  
272 expressed by:

$$273 \quad S(z,t) = a_f(h)\gamma(z)T_p \quad (8)$$

$$274 \quad T_p = ET_0(1 - e^{-kLAI}) \quad (9)$$

275 where  $a_f(h)$  represents the water stress function ( $0 \leq a_f \leq 1$ ), which reflects the reduction in root water uptake due to soil water  
276 depletion. Based on the conditions in the study area, the root water uptake model parameters were selected from the “Corn  
277 (Wesseling, 1991)” option provided by the HYDRUS-1D, as detailed in Table 3.  $\gamma(z)$  is the root water uptake distribution  
278 function ( $\text{cm}^{-1}$ ), which reflects the spatial variability of root water uptake within the vertical soil profile. In this study, a linearly  
279 decreasing function was adopted, with a maximum rooting depth of 100 cm.  $T_p$  represents the potential transpiration rate ( $\text{cm}$   
280  $\text{d}^{-1}$ ).  $ET_0$  represents the reference evapotranspiration ( $\text{cm}$ ), which can be estimated using the FAO-recommended Penman-  
281 Monteith method (Pereira et al., 2015).  $LAI$  represents the leaf area index (dimensionless), obtained from values of vegetation  
282  $LAI$  taken from Zhang et al. (2015).  $k$  represents the radiation extinction coefficient of the plant canopy (dimensionless), and  
283 is set to the default value of 0.4.

284 **Table 3. Feddes root water uptake parameters.**

$P_0(\text{cm})$	$P_{0pt}(\text{cm})$	$P_{2H}(\text{cm})$	$P_{2L}(\text{cm})$	$P_3(\text{cm})$	$r_{2H}(-)$	$r_{2L}(-)$
-15	-30	-325	-600	-8000	0.5	0.1

### 285 2.3.5 Model spin-up

286 The initial distribution of soil water content throughout the vadose zone depth is essential for obtaining reliable simulation  
287 results, as it directly influences simulated infiltration rates and actual recharge to groundwater. However, due to the  
288 considerable thickness of the vadose zone, it is not possible to provide measured initial soil water content profiles. An initial  
289 pressure head of  $h = -50$  cm was uniformly assigned to the unsaturated zone as a predefined condition. To ensure that the  
290 subsequent groundwater recharge analysis was not affected by this arbitrary starting value, it was necessary to include a  
291 sufficiently long model spin-up period (Jie et al., 2022). Accordingly, the model spin-up spanned from July 1, 2016 to July 31,  
292 2022, enabling the soil water distribution to reach a dynamic equilibrium with the meteorological boundaries and  
293 hydrogeological conditions. To verify this equilibrium state, we analyzed the time series of deep soil water content (observation  
294 depths from 20 m to 80 m) calculated during the spin-up period. As shown in Figure B, the soil water content at these depths  
295 exhibited initial fluctuations during the first 1-2 years and subsequently reached a stable dynamic equilibrium driven by the

296 surface boundary conditions, completely independent of the initial settings. Following this spin-up period, the actual  
297 groundwater recharge analysis commenced on August 1, 2022.

## 298 **2.4 Spatial interpolation**

299 Using QGIS, the locations of the 24 shallow observation wells were converted into point shapefiles, followed by projection  
300 and coordinate transformation to produce a sample distribution map suitable for geostatistical analysis. The corresponding  
301 groundwater level data for each point were integrated with the geographic attributes to create comprehensive datasets.

302 In the simulations, the infiltration process was deemed to have reached the groundwater table when initial outflow occurred at  
303 the bottom boundary of the soil profile. This duration is formally defined as the infiltration time ( $T_{inf}$ ), expressed as  $T_{inf} = t_{outflow}$   
304 -  $t_{start}$ , where  $t_{start}$  is the timestamp when the initial surface recharge event starts, and  $t_{outflow}$  is the timestamp when outflow is  
305 first recorded at the profile base.

306 Furthermore, to allow for a fair comparison between different vadose zone thicknesses ( $L$ ), we calculated the average  
307 percolation velocity ( $V_{perc}$ ) as the ratio of the vadose zone thickness to the infiltration time, i.e.,  $V_{perc} = L/T_{inf}$ .

308 Given the limited number of observation points ( $num = 24$ ) distributed over the 2,092 km<sup>2</sup> study area, robust variogram fitting  
309 required for Kriging interpolation was not feasible (Oliver and Webster, 2014). To obtain the infiltration time and rate  
310 distributions across the entire study area from the simulated 24 individual point locations by HYDRUS-1D, the Inverse  
311 Distance Weighting (IDW) method was employed for spatial interpolation of the borehole data. This approach estimates values  
312 at unsampled locations using weights inversely proportional to distances from known points, calculated as:

$$313 \quad Z(x) = \frac{\sum_{i=1}^n \frac{Z_i}{d_i^p}}{\sum_{i=1}^n \frac{1}{d_i^p}} \quad (10)$$

314 where  $Z(x)$  represents the value at the unknown point to be interpolated,  $Z_i$  indicates the value at the known point,  $d_i$  is the  
315 distance between the unknown point and the known point, and  $p$  denotes the weighting factor which is set to 2 by default.

## 316 **2.5 Multiple regression analysis**

317 To investigate the influence of vadose zone thickness and lithological characteristic on groundwater recharge efficiency, we  
318 modeled the average percolation velocities ( $V_{perc}$ , cm d<sup>-1</sup>) as the dependent variable, which directly quantifies the rate of water  
319 movement through the vadose zone and thus serves as a key indicator of recharge efficiency. Three key factors, vadose zone  
320 thickness (m), clay fraction (-), and sand fraction (-) were selected as independent variables to establish the relationships  
321 influencing percolation velocities. Since soil textural components are compositional data (i.e., clay, silt, and sand content sum  
322 to 100%), an inherent negative correlation may exist among these variables. To ensure the independence of the predictors and  
323 the robustness of the subsequent regression coefficients, Variance Inflation Factors (VIF) were calculated prior to model fitting  
324 (O'Brien, 2007).

325 
$$VIF_i = \frac{1}{1 - R_i^2} \quad (11)$$

326 where,  $R_i^2$  is the squared multiple correlation coefficient between the  $i$ th factor and all the other factors. In this study, a VIF  
327 value below 5 was adopted as the threshold indicating negligible multicollinearity.

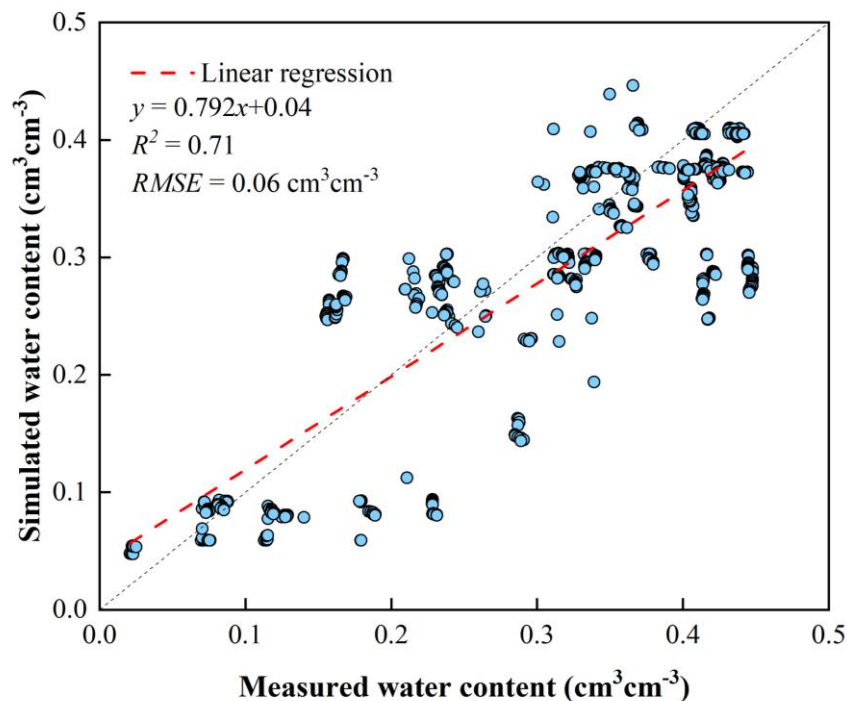
328 To account for skewed distributions and improve model fit, the natural logarithm was applied to  $V_{perc}$  and vadose zone thickness.  
329 A leave-one-out cross-validation procedure was implemented using R code. In this procedure, each observation in the dataset  
330 ( $num = 24$ ) was sequentially held out as the validation set, while the remaining  $num-1$  observations were used for regression  
331 model calibration. Within each iteration, a multiple regression model incorporating main effects and pairwise interaction terms  
332 was fitted. Model parameters were estimated using the ordinary least squares method. The regression coefficients obtained  
333 from each leave-one-out cross-validation iteration are provided in Appendix A, along with the coefficient of determination ( $R^2$ )  
334 for the training set in each iteration. Overall model performance was evaluated by aggregating predictions across all iterations  
335 to compute a validation  $R^2$  on the full dataset. Separate regression models were developed for precipitation-fed recharge (Table  
336 A.1) and riverbed recharge (Table A.2) conditions.

### 337 **3 Results**

#### 338 **3.1 Validation of soil hydraulic parameters**

339 To validate the soil hydraulic parametrization with Rosetta3 (Zhang and Schaap, 2017), we compared simulated soil water  
340 contents with measured data from the Luancheng Agricultural Ecosystem Experimental Station (Wu et al., 2023), which is  
341 situated within the study area. This station, representative of typical irrigated farmland on the NCP, features a 48-m-deep  
342 vadose zone observation caisson that enables continuous monitoring of soil water content and matric potential throughout the  
343 profile.

344 For this validation, we configured the HYDRUS-1D model using the soil profile data from this station, applying the same  
345 model setting strategy as described. Soil water content profiles at this site were measured from June to October 2021 with an  
346 interval of 1 day to 15 days, totaling 20 dates, and the measurement depth spans from 0 to 44 m. To evaluate model performance,  
347 we compared simulated soil water content at intervals of 1 m (i.e., 1, 2...44 m) across all 20 measurement dates with the  
348 corresponding observed values. As shown in Figure 4, the simulated soil water contents closely match the observed values  
349 across these depths, demonstrating strong model performance ( $R^2 = 0.71$ ,  $RMSE = 0.06 \text{ cm}^3 \text{ cm}^{-3}$ ). This agreement confirms  
350 the suitability of the Rosetta3-derived parameters for simulating vadose zone dynamics in the study region, providing reliable  
351 soil hydraulic parameters for the subsequent recharge analyses.



352

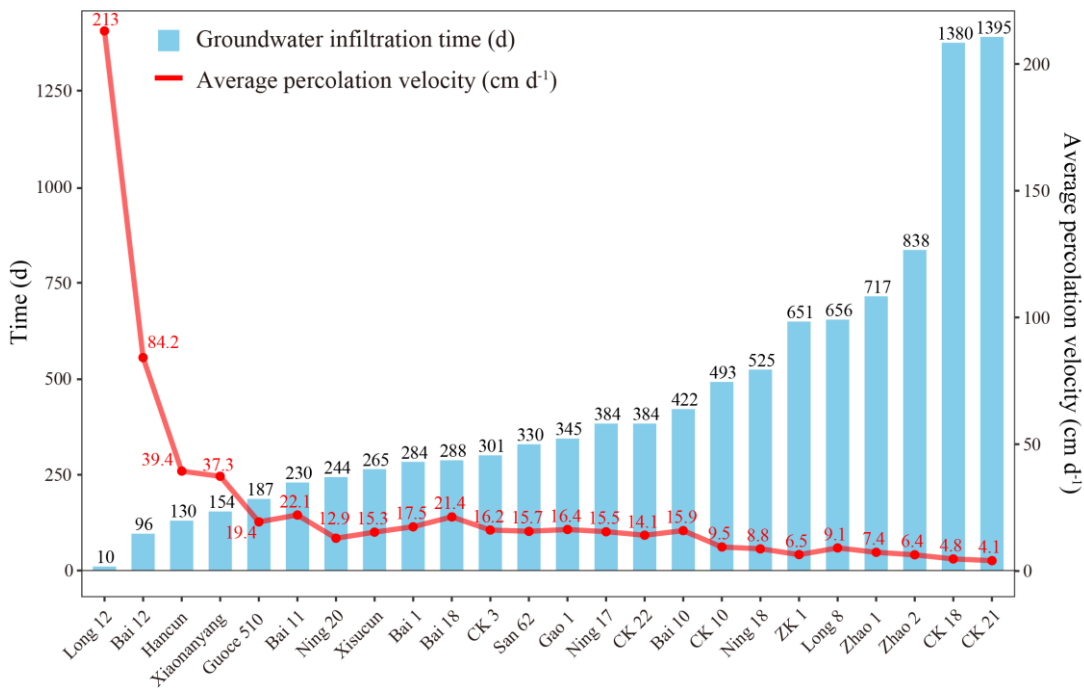
353 **Figure 4: Relationship between measured and simulated daily soil water content ( $\text{cm}^3 \text{cm}^{-3}$ ) at Luancheng Station, North China**  
 354 **Plain. The black dashed line represents the 1:1 relationship line.**

### 355 **3.2 Impact of vadose zone lithology and thickness on recharge under precipitation-fed conditions**

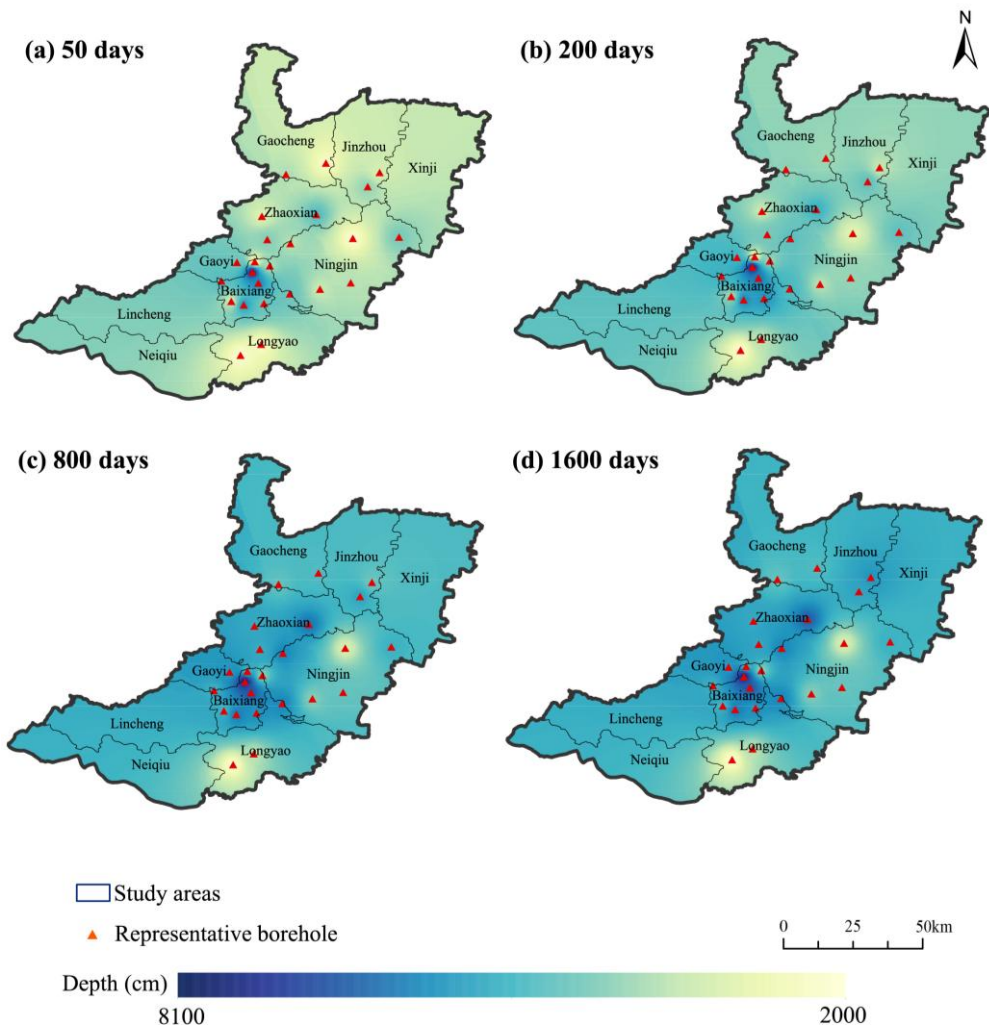
#### 356 **3.2.1 Infiltration times and average percolation velocities under precipitation recharge**

357 Simulations of the infiltration process under precipitation recharge conditions using the HYDRUS-1D model yielded estimates  
 358 of groundwater infiltration times and average percolation velocities at borehole locations across the study area (Figure 5).  
 359 These results indicated substantial variability, with an average infiltration time of 446 days across all sites. The maximum  
 360 value reached 1,395 days at borehole CK21, while the minimum was only 10 days at borehole Long 12. Infiltration times  
 361 under this recharge scenario were primarily governed by vadose zone thickness and soil lithology, reflecting the interaction  
 362 between these factors in governing water movement through the unsaturated zone. For instance, thicker vadose zones were  
 363 associated with longer infiltration times, as observed at CK21 and CK18. Even at comparable thicknesses, sites dominated by  
 364 finer-textured soils such as loam or clay (e.g., Zhao1 and ZK1) exhibited extended infiltration times. In contrast, regions with  
 365 coarser textures and higher saturated water contents, particularly in the piedmont zone of the Taihang Mountains, facilitated  
 366 faster percolation. This was evident at Long 12 in Longyao County, where infiltration reached the lower boundary in just 10  
 367 days.

368 A clear inverse relationship emerged between infiltration time (delay) and average percolation velocity, highlighting how  
 369 lithology and vadose zone thickness propagate to dictate recharge dynamics, i.e., longer delays inherently correspond to slower  
 370 velocities, as water encounters greater resistance in finer or thicker profiles. Corresponding average percolation velocities  
 371 further highlighted these lithological influences, averaging 26.4 cm d<sup>-1</sup> across the sites, with a maximum of 213.0 cm d<sup>-1</sup> at  
 372 Long 12 and a minimum of 4.1 cm d<sup>-1</sup> at CK21. This inverse pattern was particularly pronounced in heterogeneous zones,  
 373 where coarse-grained lithologies accelerated flow (high velocity, short delay) while fine-grained or layered sections impeded  
 374 it (low velocity, long delay), emphasizing the need to account for such variability in recharge predictions. To visualize the  
 375 temporal progression of recharge, Figure 6 illustrates the depth of the infiltration wetting front at selected simulation times  
 376 under the precipitation scenario. By day 50 (Figure 6a), the front had advanced beyond 20 m at most locations, with the most  
 377 rapid progression occurring in Baixiang County, where it reached approximately 40 m. By day 800 (Figure 6c), the wetting  
 378 front had typically reached the base of the vadose zone across the study area, indicating that sustained precipitation inputs  
 379 eventually overcome lithological barriers, albeit with significant lags in finer-textured or thicker profiles. These patterns  
 380 emphasize how vadose zone heterogeneity modulates recharge efficiency, with implications for the spatial distribution of  
 381 groundwater recovery in the Ningbailong depression zone.  
 382



383  
 384 **Figure 5: Groundwater infiltration time (d) and average percolation velocity (cm d<sup>-1</sup>) for locations under precipitation infiltration**  
 385 **recharge scenarios.**



386

387 **Figure 6: Depth maps of the infiltration front under the precipitation infiltration recharge scenario at (a) 50, (b) 200, (c) 800, and**  
 388 **(d) 1600 days.**

389 Based on the simulation results, a multiple regression model was developed using borehole data to investigate the logarithm  
 390 of the average percolation velocity under precipitation recharge conditions. Prior to evaluating the specific regression outcomes,  
 391 the independence of the input variables was assessed to ensure the reliability of the model. The calculated VIFs for vadose  
 392 zone thickness, clay fraction, and sand fraction were 1.018, 1.208, and 1.225, respectively. All values were well below the  
 393 established threshold of 5, indicating that multicollinearity among the predictors is negligible. Consequently, the physical  
 394 interpretation of the regression coefficients presented in the subsequent analyses is considered robust. With the model's validity  
 395 confirmed, the regression functions obtained through leave-one-out cross-validation were provided in Appendix A, including  
 396 the regression coefficients for each variable and the corresponding  $R^2$  for each calibration set. The  $R^2$  was calculated based on  
 397 the squared Pearson correlation coefficient between observed and estimated values, which emphasizes the strength of the linear

398 association. As shown in Table A.1, the  $R^2$  values for the calibration range from 0.52 to 0.83, indicating that the model structure  
399 is suitable for the data. The overall validation  $R^2$ , computed as the squared correlation between observed and estimated values  
400 across all iterations, is 0.47. Due to this small number of samples, the validation  $R^2$  is relatively modest, as limited data can  
401 introduce some uncertainty in the model's generalizability. For a better understanding of the parameter consistency, Table A.1  
402 also includes the average values and standard deviations of each regression coefficient across the calibration sets.  
403 This regression model offers significant practical utility for groundwater management and assessments in the Ningbailong  
404 depression zone and similar overexploited regions. By incorporating site-specific inputs for vadose zone thickness, clay content,  
405 and sand content into the equations, water resource policymakers can predict average percolation velocities at unsampled  
406 locations. Since infiltration time is inversely related to percolation velocity, these predictions enable estimates of recharge  
407 delays, which are essential for understanding the lag between surface inputs (e.g., precipitation events) and actual groundwater  
408 replenishment. For example, in areas with thick vadose zones and high clay content—common in the central and eastern  
409 plains—the model consistently shows negative coefficients for Depth and interactions such as Depth\*Clay and Depth\*Sand,  
410 indicating an overall trend toward slower percolation velocity and prolonged delays (potentially exceeding 1,000 days) as these  
411 factors increase. Additionally, the inclusion of quadratic terms, such as positive Depth<sup>2</sup> and Clay<sup>2</sup>, captures nonlinear effects,  
412 implying that while thickness and clay initially slow percolation strongly, this impact weakens (i.e., the rate of slowing  
413 decreases) at higher values, potentially indicating the slowing impact of greater thickness and clay content becomes weaker at  
414 higher levels of vadose zone thickness or clay content. While the model's predictive power is constrained by the small dataset,  
415 it captures key lithological controls on recharge dynamics, providing an empirical tool for preliminary assessments.

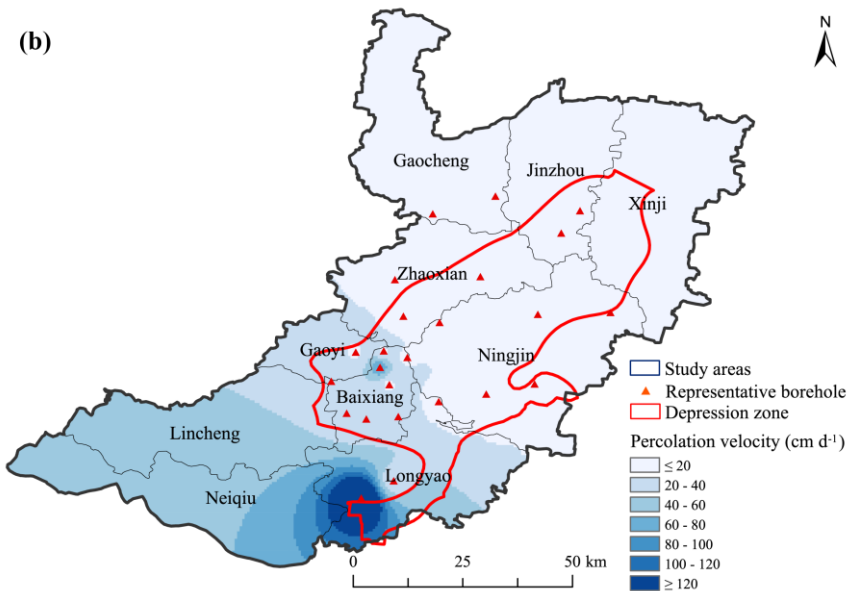
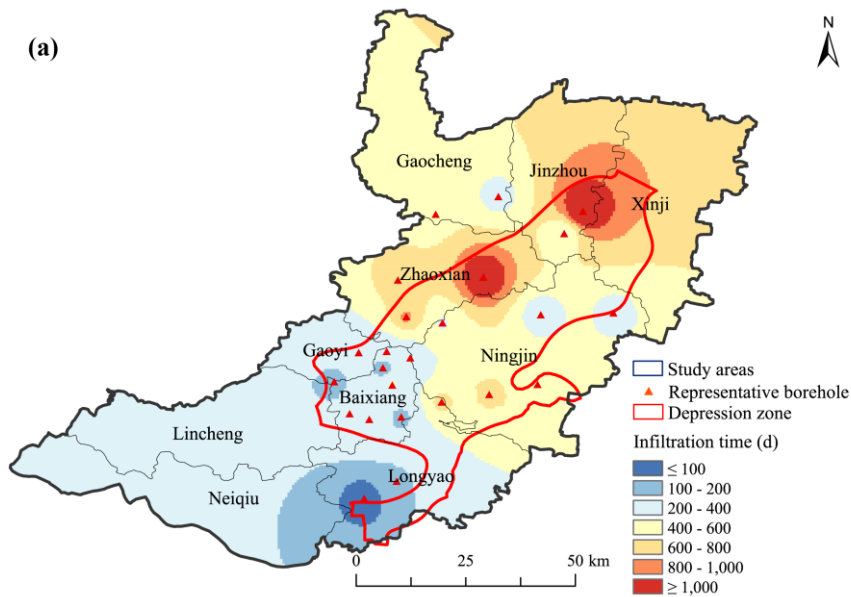
### 416 **3.2.2 Spatial distribution of infiltration times and average percolation velocities**

417 To extend the point-scale simulations to a regional perspective, we applied the inverse distance weighting (IDW) interpolation  
418 method to the HYDRUS-1D results from the 24 boreholes, generating spatial distribution maps of infiltration times and average  
419 percolation velocities across the Ningbailong depression zone (Figure 7). It is important to note that due to the sparse density  
420 of observation points, these interpolated maps should be interpreted qualitatively as indicators of general regional gradients  
421 rather than precise local predictions, particularly in areas poorly constrained by borehole data. These interpolated patterns  
422 revealed pronounced spatial variability in groundwater recharge dynamics, driven primarily by differences in vadose zone  
423 thickness and lithology. Overall, the average infiltration time in the study area is 463 days, and the average percolation velocity  
424 is 26.7 cm d<sup>-1</sup>. The infiltration times shown in Figure 7a increased progressively from the southwestern foothills of the Taihang  
425 Mountains toward the central and northern regions of the study area, forming a distinct low-to-high infiltration time gradient  
426 that mirrored topographic and geological transitions.

427 In the Taihang Mountain foothill region, exemplified by the Long 12 borehole in Longyao County, shallow groundwater depths  
428 combined with coarse-grained sand and gravel lithologies in the vadose zone enabled rapid percolation, with infiltration  
429 reaching the groundwater in only 10 days. Similarly, the southern sector of Longyao County exhibited infiltration times  
430 generally below 100 days, corresponding to average percolation velocities exceeding 100 cm d<sup>-1</sup>. These zones typically

431 coincided with locations near riverbeds or thinner vadose zones, where high-porosity and permeable soils promoted efficient  
432 downward water movement and enhanced recharge potential.

433 In contrast, infiltration times shown in Figure 7a lengthened to 200-600 days, accounting for most of the study area, including  
434 Lincheng, Baixiang, Gaoyi, Ningjin, Gaocheng, and parts of Neiqiu, Longyao, and Zhaoxian, where average percolation  
435 velocities were less than  $60 \text{ cm d}^{-1}$ . This intermediate regime reflected a shift toward moderately thicker vadose zones and  
436 finer soil textures, which reduced percolation velocities. The longest infiltration times occurred in the central and northern  
437 areas, encompassing the boundary of Jinzhou and Xinji, and eastern Zhaoxian (see the red area in Figure 7a), where durations  
438 often exceeded 1,000 days and average percolation velocities dropped below  $20 \text{ cm d}^{-1}$ . Such delays were attributable to thick  
439 vadose zones and low-permeability soils, which collectively slowed water flux and resulted in extended recharge.  
440 Consequently, these regions experience diminished recharge efficiency, limiting timely contributions to groundwater recovery  
441 in the depression zone.



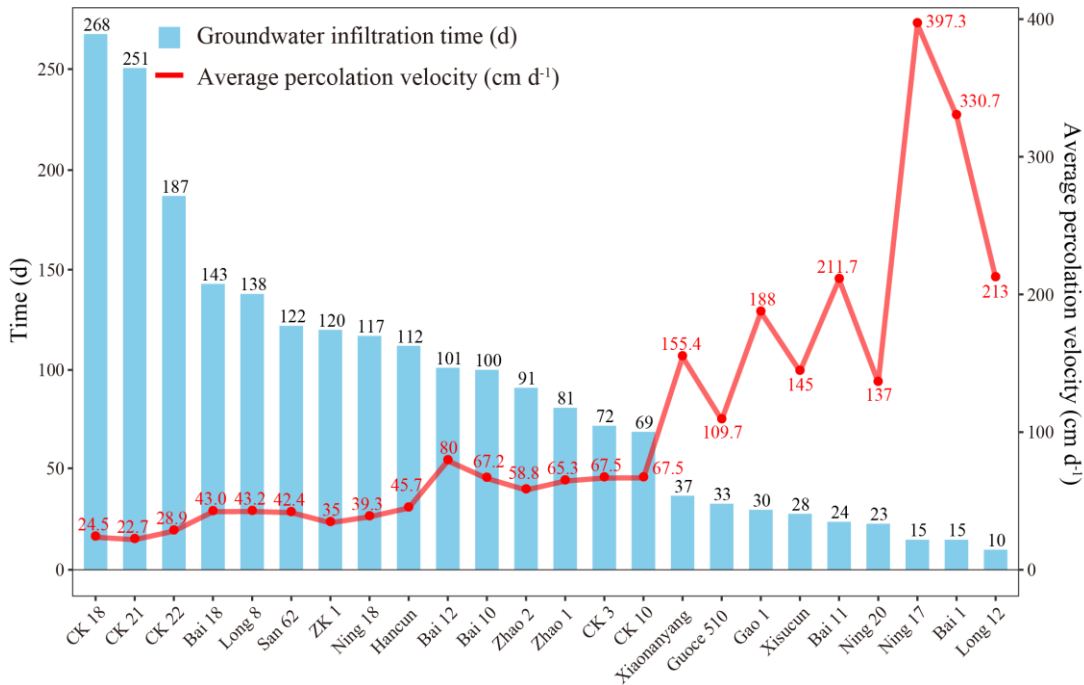
442

443 **Figure 7: (a) Infiltration times distribution under precipitation infiltration conditions, and (b) average percolation velocity**  
 444 **distribution under precipitation infiltration conditions.**

### 445 3.3 Impact of recharge sources under riverbed infiltration and comparison with precipitation-fed recharge

446 To compare recharge efficiencies, we examine infiltration under riverbed conditions using the same vadose zone profiles in  
 447 this section, quantifying times and velocities for direct comparison with precipitation-fed infiltration. Figure 8 illustrates the  
 448 groundwater infiltration time and average percolation velocity at borehole locations across the study area under riverbed  
 449 recharge conditions. The average infiltration time across all sites was 91 days, with the longest value observed at CK 18 (268

450 days) in Zhaoxian County and the shortest at Long 12 (10 days) in Longyao County. Similar to the precipitation-fed recharge  
 451 scenario, infiltration time in this case was also influenced by vadose zone thickness and soil lithological composition, with an  
 452 inverse relationship observed between velocity and lag time. The average percolation velocity across the sites was 109.1 cm  
 453 d<sup>-1</sup>, ranging from a minimum of 24.5 cm d<sup>-1</sup> at CK 18 in Zhaoxian County to a maximum of 397.3 cm d<sup>-1</sup> at Ning 17 in Ningjin  
 454 County.  
 455



456  
 457 **Figure 8: Groundwater infiltration time (d) and average percolation velocity (cm d<sup>-1</sup>) for locations under riverbed infiltration**  
 458 **recharge scenarios.**

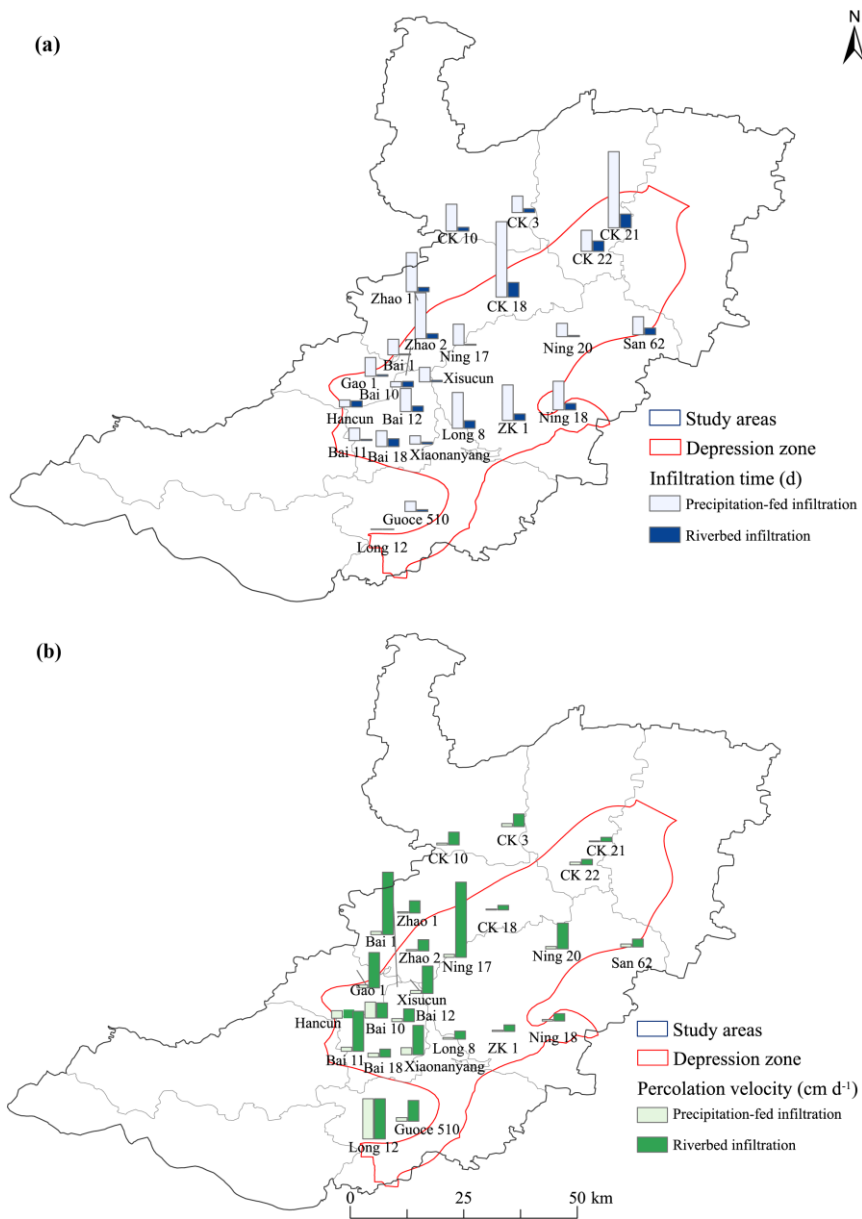
459 Based on the simulation results, a multiple regression model was developed using borehole data to characterize the average  
 460 percolation velocity under riverbed recharge conditions, following the same methodology as for the precipitation-fed model.  
 461 The estimated regression coefficients, as well as the average values and standard deviations of the coefficients, are listed in  
 462 Table A.2, with calibration *R*<sup>2</sup> values ranging from 0.76 to 0.87, indicating a good fit comparable to the precipitation model.  
 463 Unlike the precipitation-fed model, the regression equation does not include quadratic terms for depth or clay (i.e., no depth<sup>2</sup>  
 464 or clay<sup>2</sup> terms), as we found that removing these terms improved the fitting to the regression curves. The overall validation *R*<sup>2</sup>  
 465 (squared correlation between observed and predicted values) is 0.47, affirming the model's utility despite the small sample  
 466 size, though this modest value underscores the need for larger datasets to prevent the overfitting and reduce prediction  
 467 variability.

468 Similar to the precipitation model, this regression work enables rapid estimation of percolation velocities, and thus recharge  
 469 delays, using vadose zone thickness, clay content, and sand content, but it reveals distinct dynamics under riverbed conditions.

470 For instance, Table A.2 shows consistently positive coefficients for the main effect of depth (averaging around 1.44 across  
471 folds), contrasting with the negative coefficients in Table A.1 (averaging around -15.94), indicating that thicker vadose zones  
472 facilitate higher log-transformed velocities under constant-head infiltration. This aligns with the observed higher average  
473 velocities (109.1 cm d<sup>-1</sup> vs. 26.4 cm d<sup>-1</sup> for precipitation), implying shorter delays even in clay-rich zones, potentially by 4–5  
474 times based on coefficient magnitudes from the log transformation. Such patterns highlight riverbed recharge’s resilience to  
475 lithological barriers, making this approach particularly valuable for optimizing managed aquifer recharge (MAR) strategies,  
476 e.g., identifying appropriate sites where artificial riverbed-like basins could accelerate recovery. Future enhancements with  
477 more boreholes could refine these insights, enabling probabilistic delay forecasting under varying flood scenarios.

478 In order to analyze the impact of different recharge sources on groundwater recharge, we compared the infiltration times and  
479 average percolation velocities at the same boreholes under two infiltration conditions, as shown in Figure 9. These comparisons  
480 enabled us to assess the recharge efficiency and highlight the differences in infiltration time and spatial scope between the two  
481 conditions. Overall, the infiltration duration of the riverbed was shorter and more efficient. However, there were also certain  
482 differences based on location. For example, in the southwestern part of the Ningbailong groundwater depression zone, at the  
483 Long 12, Hancun, and Bai 10 in Figure 9b, the average infiltration velocity of precipitation and riverbed recharge were similar.  
484 While in most of the depression areas, the central and northern parts, the differences in the two infiltration recharge efficiencies  
485 were significant, such as Ning 17, Bai 1, and Ning 20 shown in Figure 9b.

486 In general, riverbed recharge exerted a stronger influence on groundwater, particularly in localized areas near channels,  
487 although its overall spatial footprint remained constrained. Precipitation recharge, by contrast, induced slower groundwater  
488 recharge but contributed over a broader regional scale, highlighting its role in widespread, albeit delayed, groundwater recovery  
489 within the depression zone.



490

491 **Figure 9: Comparison of (a) infiltration time and (b) percolation velocities between two recharge sources within the study area.**

492 **4 Discussion**

493 **4.1 Vadose Zone Controls on Groundwater Recharge Efficiency**

494 In this study, we quantified infiltration times and percolation velocity through the vadose zone at boreholes within the

495 Ningbailong groundwater depression zone, using measured borehole data and hydrometeorological records starting from July

496 1, 2022. This approach enabled the quantification of recharge efficiency by precipitation-fed infiltration through soils and  
497 riverbed infiltration. The findings demonstrate that the development of the Ningbailong depression zone arises not only from  
498 anthropogenic overexploitation but also from inherent geological constraints, including vadose zone lithology and thickness,  
499 which play a critical role in limiting natural recharge. For example, the extended infiltration times observed at the zone's center  
500 in Ningjin County, are consistent with the findings of Zhao et al. (2020).

501 To further elucidate these mechanisms, the multiple regression models developed for percolation velocities under both  
502 precipitation-fed and riverbed conditions demonstrate that the selected independent variables, including vadose zone thickness,  
503 clay content, and sand content, exhibit satisfactory explanatory power. The results highlight that unsaturated zone thickness  
504 and lithological characteristics are the dominant factors controlling groundwater recharge in the Ningbailong depression zone,  
505 where thicker profiles and finer textures impede percolation, while coarser sands promote faster flow. Key differences between  
506 the two infiltration conditions include nonlinear dynamics in precipitation-fed recharge (captured by quadratic terms),  
507 suggesting diminishing slowing effects at extreme thickness or clay levels, implying some resilience in severely groundwater  
508 depression zones. In contrast, riverbed recharge shows more linear patterns, enabling faster velocities and shorter delays. This  
509 highlights riverbed recharge's potential to bypass constraints more effectively than precipitation.

#### 510 **4.2 Recharge Efficiency and Implications**

511 Our analysis demonstrates distinct differences in recharge efficacy between precipitation and riverbed sources. Under  
512 equivalent vadose zone and temporal conditions, riverbed infiltration, i.e., simulated with a constant head boundary, exhibited  
513 markedly greater recharge efficacy than precipitation-fed infiltration, which is in line with the studies by Nan et al. (2024).  
514 Regarding contributions to total recharge volume, while precipitation-fed infiltration dominates the study area (covering 99.65%  
515 of the region compared to the 0.35% river area in this region), its lower average percolation velocity ( $26.4 \text{ cm d}^{-1}$ ) contrasts  
516 sharply with the higher velocity for riverbed ( $109.1 \text{ cm d}^{-1}$ ). Based on these percolation velocities, the per-unit-area recharge  
517 efficiency from riverbed is approximately 4.1 times higher. Thus, despite its limited areal coverage, riverbed infiltration serves  
518 as a more efficient recharge approach in terms of vertical percolation velocities. In mountain-front regions with coarse-grained  
519 soils, both infiltration types exhibit velocities exceeding  $100 \text{ cm d}^{-1}$ , yet riverbed infiltration remains superior. Strategically  
520 expanding riverbed-like infiltration zones in such areas could enhance total recharge volume and expedite groundwater  
521 recovery in overexploited aquifers.

522 However, given the North China Plain's intensive agriculture and severe land scarcity, constructing new large-scale  
523 infiltration basins is largely impractical. Instead, our percolation velocity data demonstrate that existing seasonal dry riverbeds  
524 can serve as highly efficient, natural infiltration zones. By prioritizing riverbed infiltration, particularly in foothill alluvial fan  
525 areas with coarse-grained sediments (e.g., near boreholes Long 12, Bai 1), this strategy can achieve rapid groundwater  
526 replenishment without sacrificing valuable arable land or requiring high land acquisition costs.

### 527 4.3 Limitations and Future Perspectives

528 Several limitations in the current analysis point to avenues for refinement in subsequent investigations. First, the model inputs  
529 for precipitation boundary conditions started in August 2022, when the flood season was heavy, potentially biasing estimates  
530 toward high-intensity events. Considering the pronounced interannual variability in precipitation patterns, differences in initial  
531 soil water content within the thick vadose zone inevitably led to variations in infiltration and recharge across different years.  
532 Future research should categorize hydrological years (e.g., wet, normal, and dry) using frequency-based analyses and simulate  
533 water flux variations under these varied regimes, thereby providing a more comprehensive understanding of infiltration time  
534 variability in the vadose zone.

535 Second, due to the challenges in directly measuring the hydraulic parameters and actual soil water content of the thick  
536 unsaturated zone in the study area, the current parameters were derived from the Rosetta3 model, which inherently generalizes  
537 lithological properties to some degree. Such estimations may diverge from site-specific field values, introducing potential  
538 uncertainties into the simulation results. In addition to soil hydraulic parameters, the representation of vegetation dynamics  
539 plays a critical role in partitioning precipitation into infiltration and evapotranspiration. In this study, root water uptake was  
540 simulated using the default parameters and literature-based LAI values. However, recent advancements have demonstrated  
541 that the assimilation of high-resolution remote sensing data, such as Sentinel-based LAI, can significantly enhance the  
542 modelling of surface water-groundwater interactions, particularly in agricultural irrigation districts ([Zafarmomen et al., 2024](#)).  
543 These studies highlight that incorporating dynamic, spatially distributed vegetation data by relying on data assimilation  
544 frameworks can effectively reduce uncertainties in evapotranspiration estimation and, consequently, improve the accuracy of  
545 deep percolation and recharge fluxes. Future investigations could benefit from integrating field experiments for parameter  
546 calibration and adopting remote sensing assimilation techniques to refine upper boundary conditions, collectively enhancing  
547 the robustness of vadose zone modelling in similar hydrogeological settings.

548 Third, certain simplifications in the model structure may introduce biases into the calculated lag times. Specifically, our model  
549 does not account for three complex processes, i.e., preferential flow, dynamic riverbed clogging, and lateral flow. For instance,  
550 the assumption of homogeneous matrix flow omits preferential flow paths (e.g., macropores or fractures). Since these pathways  
551 allow water to rapidly bypass the soil matrix, neglecting them means our simulated lag times are likely overestimated (i.e.,  
552 actual recharge is faster) (Li et al., 2025). Additionally, the model assumes static soil hydraulic properties, neglecting dynamic  
553 riverbed clogging (such as physical sedimentation). Because clogging typically reduces surface permeability over time,  
554 omitting this process likely leads to an underestimation of the true lag times for riverbed recharge. Furthermore, the HYDRUS-  
555 1D model is restricted to strictly vertical flow, neglecting lateral fluxes. As highlighted by recent comprehensive studies, the  
556 limitations of strictly 1D conceptualizations become significantly more pronounced in highly heterogeneous domains (Fan et  
557 al., 2019; Chen et al., 2022). Particularly in our study area, when infiltrating water encounters low-permeability stratigraphic  
558 interfaces at depth (e.g., clay layers), temporary perched conditions can induce localized lateral redistribution (Vereecken et  
559 al., 2019). In reality, this lateral flow extends the travel path of infiltrating water, suggesting that our strictly 1D simulation

560 may underestimate the actual lag times (Isch et al., 2022). However, implementing a multi-dimensional (2D/3D) model  
561 requires detailed data on horizontal stratigraphic continuity, which is rarely available at the regional scale and could introduce  
562 substantial uncertainty. Besides, the flat topography and deep water tables across the North China Plain result in a vertical  
563 hydraulic gradient that far exceeds horizontal gradients. Previous modeling and field studies have successfully demonstrated  
564 that 1D vertical flow effectively captures the dominant mechanisms controlling groundwater recharge through the thick vadose  
565 zone in this region (Huo et al., 2014; Min et al., 2015; Cao et al., 2016). Consequently, despite potential biases, we ultimately  
566 chose the HYDRUS-1D model as the robust and practical approach for simulating regional recharge dynamics in this study.  
567 Finally, due to the limited number of observational boreholes (only 24), the regression equations performed less effectively on  
568 the validation dataset, reflecting overfitting and prediction variability. For the same reason, while IDW interpolation provided  
569 a useful spatial representation of recharge patterns, it did not quantify estimation errors. Consequently, the prediction accuracy  
570 may be lower in regions where sampling points are sparse. Future research should expand datasets and validate with field  
571 experiments to enhance accuracy. Ultimately, these models inform adaptive strategies, such as prioritizing managed aquifer  
572 recharge in high-permeability areas to accelerate recovery.

## 573 **5 Conclusions**

574 This study provides a comprehensive analysis of groundwater recharge dynamics in the Ningbailong depression zone, a typical  
575 groundwater overexploited area in the North China Plain. Using HYDRUS-1D simulations informed by site-specific borehole  
576 lithology, vadose zone thicknesses, and hydro-meteorological data, we quantified infiltration times and percolation velocities  
577 under precipitation-fed and riverbed recharge sources. Empirical regression equations were derived to relate these percolation  
578 velocities to key vadose zone properties (e.g., thickness and lithology), facilitating spatial extrapolation and elucidating  
579 dominant controls on recharge efficiency in deep, heterogeneous vadose zones. The main conclusions are summarized below:

580 1 Precipitation recharge, while widespread, exhibits prolonged infiltration times averaging 446 days and percolation  
581 velocities of  $26.4 \text{ cm d}^{-1}$ , leading to lower overall efficiency and delayed groundwater replenishment. In contrast, riverbed  
582 infiltration is markedly faster and more concentrated, with average infiltration times of 91 days and percolation velocity  
583 of  $109.1 \text{ cm d}^{-1}$  under equivalent lithological conditions, highlighting its superior efficacy for rapid groundwater recovery.  
584 This disparity highlights the potential of managed aquifer recharge strategies leveraging riverbeds, particularly in  
585 overexploited regions where precipitation alone cannot balance extraction rates.

586 2 Recharge dynamics are profoundly modulated by vadose zone characteristics, with thicker profiles ( $>50 \text{ m}$ ) and finer-  
587 textured soils (e.g., clays and loams) extending infiltration times up to 1,395 days (averaging 446 days but varying from  
588 10 days in coarse-grained zones to over a thousand days in finer ones) and slowing velocities below  $5 \text{ cm d}^{-1}$  under  
589 precipitation-fed condition, while coarser sands facilitate faster infiltration ( $>200 \text{ cm d}^{-1}$ ). These thicker profiles and fine-  
590 textured soils increase recharge lags, worsening groundwater depletion by decoupling surface inputs from aquifer  
591 responses, potentially delaying recovery by years. In the Ningbailong depression zone, such geological constraints,

592 combined with historical overexploitation likely contribute to the persistence of the depression,-keeping the water supply  
593 and demand out of balance.

594 3 Recharge processes display pronounced spatial variability, with infiltration times increasing and velocities decreasing  
595 from the western Taihang Mountain foothills (e.g., <100 days in permeable, thinner zones) toward the central and eastern  
596 plains (>1,000 days in thicker, finer lithologies). This gradient emphasizes the foothills as likely prime locations for  
597 managed aquifer recharge strategies, due to their high-permeability sediments that enable efficient percolation.

598 4 Empirical regression equations were derived through multiple regression analysis with leave-one-out cross-validation to  
599 predict percolation velocities based on vadose zone thickness (log-transformed), clay content, and sand content. The  
600 regression equations exhibit good calibration performance, with  $R^2$  values averaging around 0.7 for precipitation-fed  
601 recharge and 0.8 for riverbed recharge. However, the overall validation  $R^2$  values are modest (0.47 for both precipitation-  
602 fed and riverbed), reflecting the limited sample size (24 boreholes), which may contribute to prediction variability and  
603 potential overfitting. Expanding the dataset with additional boreholes, would potentially enhance model robustness,  
604 generalizability, and predictive accuracy. Nonetheless, these equations provide valuable preliminary insights into the  
605 influence of lithology and thickness on recharge dynamics, enabling estimates of delays and efficiencies at unsampled  
606 sites to inform groundwater management strategies in depression zones.

607 With respect to recharge regimes, both precipitation-fed infiltration and riverbed infiltration are feasible approaches in the  
608 southwestern part of the study area, where their efficiencies are comparable. In contrast, across most of the central and northern  
609 regions, riverbed infiltration exhibits a substantially higher efficiency than precipitation infiltration. Given the region's severe  
610 land-use constraints, we recommend prioritizing existing dry river channels for floodwater capture to achieve rapid  
611 groundwater recovery without occupying valuable agricultural land. For practical groundwater recovery management, it is  
612 essential to incorporate vadose zone lags and heterogeneity into the strategies, with these insights holding potential to inform  
613 sustainable management in analogous groundwater depression zones.

#### 614 **Data availability**

615 Data will be made available on request.

#### 616 **Author contributions**

617 Shenghao XU contributed to the conceptualization, data curation, formal analysis, methodology, software, visualization, and  
618 writing (original draft preparation). Yonggen Zhang contributed to the conceptualization, funding acquisition, methodology,  
619 project administration, supervision, and writing (review and editing). Xinwang Li contributed to the data curation, and  
620 investigation. Jianzhu Li contributed to the conceptualization, funding acquisition, supervision, and writing (review and  
621 editing). Wenhao Shi contributed to the software, and visualization. Shaowei Lian contributed to the data curation, and

622 resources. Lei Li contributed to the data curation, and investigation. Lutz Weihermüller contributed to the methodology, and  
 623 writing (review and editing). Marcel Schaap contributed to the methodology, and writing (review and editing).

#### 624 **Competing interests**

625 The authors have the following competing interests: Yonggen Zhang is a member of the editorial board of Hydrology and  
 626 Earth System Sciences.

#### 627 **Acknowledgments**

628 This work was supported by the National Natural Science Foundation of China (grant numbers: 42472327, 42077168) and the  
 629 National Key R&D Program of China (grant number: 2023YFC3006503). Schaap was supported, in part, by USDA-NIFA W-  
 630 4188 “Soil Water and Environmental Physics to Sustain Agriculture and Natural resources” and USDA-NRCS Award  
 631 NR233A750023C022.

#### 632 **Appendix A. Regression coefficients obtained from the multiple regression model with leave-one-out cross-validation.**

633 Depth represents the logarithm of the vadose zone thickness (m), clay represents clay fraction (-), and sand represents sand  
 634 fraction (-).  $R^2_{cal}$  and  $R^2_{val}$  indicate the coefficient of determination for the calibration and validation datasets.

635 **Table A.1. Regression coefficient of the multiple regression model for the logarithm of the average percolation velocity (cm d<sup>-1</sup>)**  
 636 **under precipitation recharge conditions.**

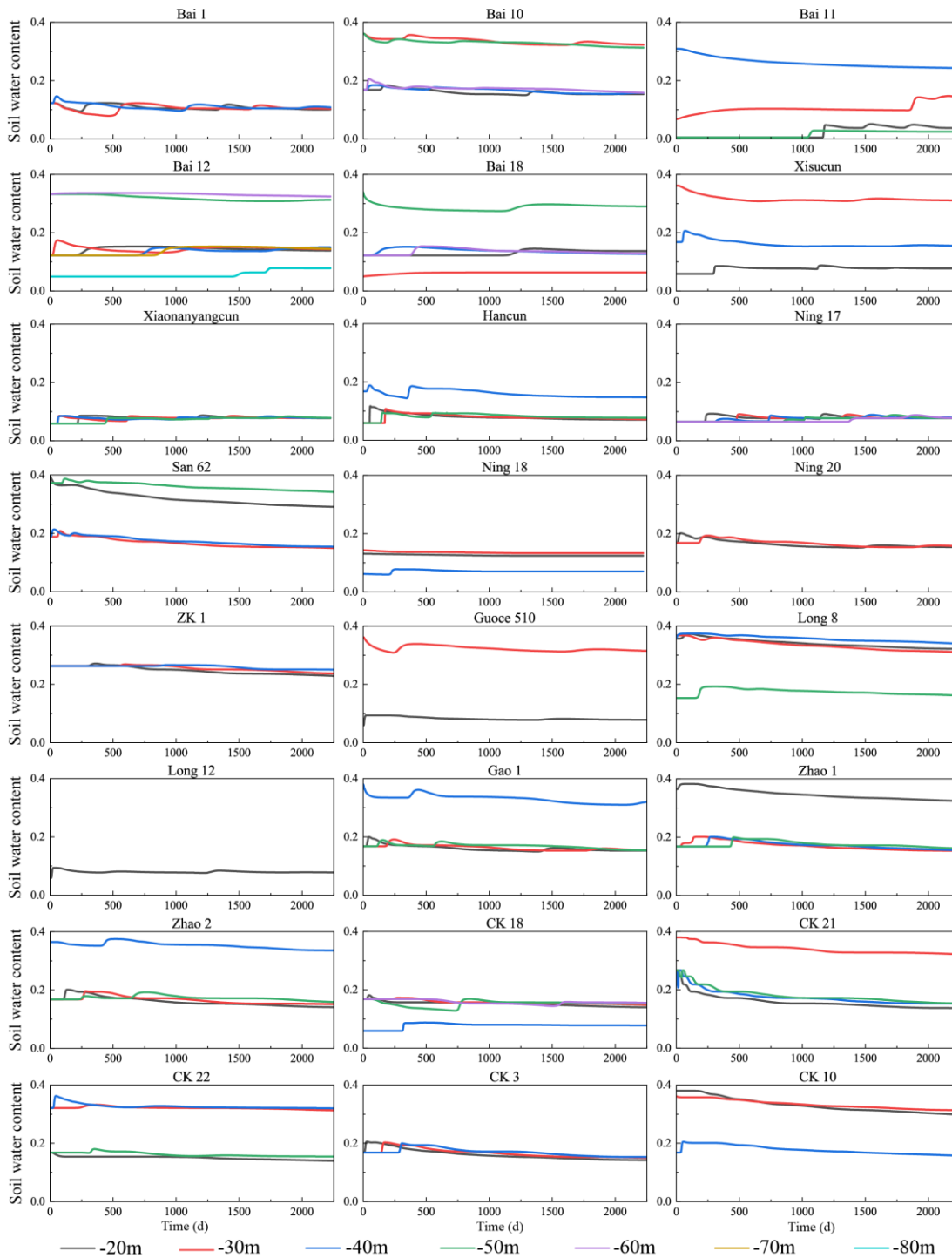
Set	Intercept	Depth	Clay	Sand	Depth*Clay	Depth*Sand	Depth <sup>2</sup>	Clay <sup>2</sup>	R <sup>2</sup> cal	R <sup>2</sup> val
1	24.86	-15.77	54.10	14.09	-14.84	-3.63	2.60	6.79	0.71	
2	24.28	-15.49	54.33	14.25	-14.91	-3.67	2.57	6.86	0.71	
3	28.18	-17.29	52.78	12.72	-14.46	-3.27	2.77	6.69	0.72	
4	21.83	-13.32	50.61	11.03	-13.79	-2.80	2.16	6.11	0.66	
5	24.89	-15.77	53.98	14.04	-14.81	-3.61	2.60	6.80	0.70	
6	8.53	-8.16	70.14	17.19	-18.82	-4.41	1.72	6.74	0.73	
7	21.07	-14.50	53.60	19.50	-14.64	-5.07	2.53	6.29	0.74	
8	30.44	-18.57	53.01	13.57	-15.01	-3.57	2.97	8.59	0.83	0.47
9	26.99	-16.55	54.57	11.43	-15.02	-2.93	2.66	7.26	0.71	
10	27.20	-16.80	53.14	12.95	-14.61	-3.32	2.71	7.04	0.71	
11	18.38	-12.90	54.93	17.99	-15.05	-4.59	2.29	6.62	0.72	
12	22.61	-14.71	59.32	12.76	-16.11	-3.29	2.47	6.58	0.71	
13	30.63	-17.44	51.23	6.90	-14.28	-1.88	2.67	7.53	0.71	
14	20.30	-14.54	55.91	20.02	-15.34	-5.12	2.58	7.14	0.73	
15	24.74	-15.72	54.08	14.20	-14.84	-3.66	2.60	6.80	0.70	

Set	Intercept	Depth	Clay	Sand	Depth*Clay	Depth*Sand	Depth <sup>2</sup>	Clay <sup>2</sup>	R <sup>2</sup> cal	R <sup>2</sup> val
16	36.26	-21.60	58.03	13.70	-15.77	-3.51	3.34	6.56	0.52	
17	24.29	-15.43	55.41	13.41	-15.28	-3.45	2.55	7.43	0.71	
18	21.57	-14.32	55.18	15.73	-15.06	-4.06	2.45	6.29	0.71	
19	21.23	-14.12	55.36	15.46	-15.11	-3.97	2.42	6.31	0.72	
20	39.71	-22.33	43.45	7.49	-11.83	-1.89	3.29	5.33	0.70	
21	29.08	-17.53	49.19	11.92	-13.30	-3.02	2.76	5.35	0.70	
22	28.09	-17.22	50.59	13.04	-14.37	-3.39	2.77	11.34	0.71	
23	28.21	-17.33	52.94	12.88	-14.63	-3.32	2.78	7.42	0.72	
24	23.82	-15.24	54.62	14.20	-14.97	-3.67	2.54	6.72	0.70	
Average Value	25.30	-15.94	54.19	13.77	-14.87	-3.55	2.62	6.94	/	/
Standard Deviation	6.10	2.80	4.59	3.07	1.19	0.78	0.33	1.16	/	/

637 Table A.2. Regression coefficient of the multiple regression model for the logarithm of the average percolation velocity (cm d<sup>-1</sup>)  
638 under riverbed recharge conditions.

Set	Intercept	Depth	Clay	Sand	Depth*Clay	Depth*Sand	Clay*Sand	R <sup>2</sup> cal	R <sup>2</sup> val
1	-0.56	1.42	-43.51	5.76	10.46	-1.95	8.86	0.77	
2	-0.63	1.46	-43.50	5.29	10.37	-1.88	9.74	0.78	
3	-1.23	1.64	-44.07	6.77	10.45	-2.27	9.80	0.81	
4	-2.31	1.91	-41.02	7.23	9.72	-2.39	9.68	0.78	
5	1.34	0.92	-45.57	3.32	10.98	-1.35	9.42	0.80	
6	-1.17	1.58	-36.49	4.96	8.64	-1.79	10.11	0.80	
7	-0.99	1.56	-43.97	6.35	10.48	-2.17	9.81	0.78	
8	-0.28	1.37	-45.09	5.24	10.74	-1.87	10.53	0.79	
9	1.82	0.79	-40.51	0.31	9.77	-0.53	8.40	0.77	
10	0.07	1.26	-43.63	4.44	10.44	-1.64	9.54	0.79	
11	1.95	0.82	-39.42	-1.16	9.39	-0.32	9.59	0.87	
12	-0.47	1.46	-66.58	15.43	16.05	-4.46	10.09	0.81	
13	-5.29	2.57	-40.34	12.39	9.69	-3.60	9.32	0.79	0.47
14	0.65	1.13	-43.80	3.68	10.47	-1.47	9.52	0.78	
15	-1.64	1.72	-44.08	7.29	10.58	-2.40	9.27	0.78	
16	1.77	0.84	-56.79	1.74	13.76	-0.98	9.41	0.76	
17	-0.64	1.46	-44.27	5.79	10.55	-2.02	9.90	0.78	
18	-0.63	1.46	-43.59	5.53	10.40	-1.95	9.67	0.79	
19	-0.32	1.37	-43.36	5.03	10.37	-1.81	9.47	0.79	
20	-1.14	1.59	-41.73	6.20	9.97	-2.11	9.14	0.76	
21	-1.00	1.55	-41.00	5.77	9.82	-2.00	8.73	0.77	
22	-1.51	1.81	-44.51	6.74	9.63	-2.40	15.30	0.80	
23	-0.48	1.42	-43.62	5.33	10.41	-1.89	9.67	0.78	
24	-0.39	1.40	-43.47	5.14	10.38	-1.85	9.57	0.78	

<b>Set</b>	<b>Intercept</b>	<b>Depth</b>	<b>Clay</b>	<b>Sand</b>	<b>Depth*Clay</b>	<b>Depth*Sand</b>	<b>Clay*Sand</b>	<b>R<sup>2</sup> cal</b>	<b>R<sup>2</sup> val</b>
Average Value	-0.54	1.44	-44.33	5.61	10.56	-1.96	9.77	/	/
Standard Deviation	1.51	0.38	5.91	3.31	1.47	0.84	1.26	/	/



640

641 Figure B: Temporal variation of deep vadose zone soil water content during model spin-up period.

## 642 References

- 643 Arnold, J. G., Moriasi, D. N., Gassman, P. W., Abbaspour, K. C., White, M. J., Srinivasan, R., Santhi, C., Harmel, R. D., Van  
644 Griensven, A., an Liew, M. W. V., Kannan, N., and Jha, M. K.: SWAT: model use, calibration, and validation, *Trans. ASABE*,  
645 55, 1491–1508, <https://doi.org/10.13031/2013.42256>, 2012.
- 646 Assefa, K. A. and Woodbury, A. D.: Transient, spatially varied groundwater recharge modeling, *Water Resour. Res.*, 49, 4593–  
647 4606, <https://doi.org/10.1002/wrcr.20332>, 2013.
- 648 Assouline, S.: Infiltration into soils: conceptual approaches and solutions, *Water Resour. Res.*, 49, 1755–1772,  
649 <https://doi.org/10.1002/wrcr.20155>, 2013.
- 650 Bierkens, M. F. P., Sutanudjaja, E. H., and Wanders, N.: Large-scale sensitivities of groundwater and surface water to  
651 groundwater withdrawal, *Hydrol. Earth Syst. Sci.*, 25, 5859–5878, <https://doi.org/10.5194/hess-25-5859-2021>, 2021.
- 652 Cao, G. L., Scanlon, B. R., Han, D. M., and Zheng, C. M.: Impacts of thickening unsaturated zone on groundwater recharge  
653 in the North China Plain, *J. Hydrol.*, 537, 260–270, <https://doi.org/10.1016/j.jhydrol.2016.03.049>, 2016.
- 654 Chen, L., Šimůnek, J., Bradford, S. A., Ajami, H., and Meles, M. B.: A computationally efficient hydrologic modeling  
655 framework to simulate surface–subsurface hydrological processes at the hillslope scale, *J. Hydrol.*, 614, 128539,  
656 <https://doi.org/10.1016/j.jhydrol.2022.128539>, 2022.
- 657 Chen, X. Z., Wang, P. X., Muhammad, T., Xu, Z. C., and Li, Y. K.: Subsystem-level groundwater footprint assessment in  
658 North China Plain – the world’s largest groundwater depression cone, *Ecol. Indic.*, 117, 106662,  
659 <https://doi.org/10.1016/j.ecolind.2020.106662>, 2020.
- 660 Christine, S. and Gerhard, K.: The vadose zone – a semi-aquatic ecosystem, in: *Encyclopedia of Inland Waters (Second*  
661 *Edition)*, edited by: Thomas, M. and Klement, T., Elsevier, 331–338, 2022. Dadgar, M. A., Nakhaei, M., Porhemmat, J., Biswas,  
662 A., and Rostami, M.: Transient potential groundwater recharge under surface irrigation in a semiarid environment: an  
663 experimental and numerical study, *Hydrol. Process.*, 32, 3771–3783, <https://doi.org/10.1002/hyp.13287>, 2018.
- 664 Dafny, E. and Šimůnek, J.: Infiltration in layered loessial deposits: revised numerical simulations and recharge assessment, *J.*  
665 *Hydrol.*, 538, 339–354, <https://doi.org/10.1016/j.jhydrol.2016.04.029>, 2016.
- 666 Di Ciacca, A., Wilson, S., Durney, P., Stecca, G., and Wöhling, T.: Model simplification to simulate groundwater recharge  
667 from a perched gravel-bed river, *J. Hydrol.*, 643, 132016, <https://doi.org/10.1016/j.jhydrol.2024.132016>, 2024.
- 668 Dillon, P., Stuyfzand, P., Grischek, T., Lluria, M., Pyne, R. D. G., Jain, R. C., Bear, J., Schwarz, J., Wang, W., Fernandez, E.,  
669 Stefan, C., Pettenati, M., Van der Gun, J., Sprenger, C., Massmann, G., Scanlon, B. R., Xanke, J., Jokela, P., Zheng, Y.,  
670 Rossetto, R., Shamruk, M., Pavelic, P., Murray, E., Ross, A., Bonilla Valverde, J. P., Palma Nava, A., Ansems, N., Posavec,  
671 K., Ha, K., Martin, R., and Sapiano, M.: Sixty years of global progress in managed aquifer recharge, *Hydrogeol. J.*, 27, 1–30,  
672 <https://doi.org/10.1007/s10040-018-1841-z>, 2019.
- 673 Fan, Y., Clark, M., Lawrence, D. M., Swenson, S., Band, L. E., Brantley, S. L., Brooks, P. D., Dietrich, W. E., Flores, A.,  
674 Grant, G., Kirchner, J. W., Mackay, D. S., McDonnell, J. J., Milly, P. C. D., Sullivan, P. L., Tague, C., Ajami, H., Chaney, N.,

675 Hartmann, A., Hazenberg, P., McNamara, J., Pelletier, J., Perket, J., Rouholahnejad-Freund, E., Wagener, T., Zeng, X.,  
676 Beighley, E., Buzan, J., Huang, M., Livneh, B., Mohanty, B. P., Nijssen, B., Safeeq, M., Shen, C., Van Verseveld, W., Volk,  
677 J., and Yamazaki, D.: Hillslope hydrology in global change research and Earth system modeling, *Water Resour. Res.*, 55,  
678 1737–1772, <https://doi.org/10.1029/2018WR023903>, 2019.

679 Ganot, Y., Holtzman, R., Weisbrod, N., Nitzan, I., Katz, Y., and Kurtzman, D.: Monitoring and modeling infiltration–recharge  
680 dynamics of managed aquifer recharge with desalinated seawater, *Hydrol. Earth Syst. Sci.*, 21, 4479–4493,  
681 <https://doi.org/10.5194/hess-21-4479-2017>, 2017.

682 Gao, Y., Fu, Y. C., Chen, J. J., and Sun, D. A.: A novel equation for simulating the bimodal soil–water retention curve of  
683 unsaturated soils, *Acta Geotech.*, 19, 5347–5362, <https://doi.org/10.1007/s11440-024-02233-y>, 2024.

684 Huo, S. Y., Jin, M. G., Liang, X., and Lin, D.: Changes of vertical groundwater recharge with increase in thickness of vadose  
685 zone simulated by one-dimensional variably saturated flow model, *J. Earth Sci.*, 25, 1043–1050,  
686 <https://doi.org/10.1007/s12583-014-0486-7>, 2014.

687 Isch, A., Coquet, Y., Abbar, B., Aldana, C., Abbas, M., Bruand, A., and Azaroual, M.: A comprehensive experimental and  
688 numerical analysis of water flow and travel time in a highly heterogeneous vadose zone, *J. Hydrol.*, 610, 127875,  
689 <https://doi.org/10.1016/j.jhydrol.2022.127875>, 2022.

690 Jasechko, S. and Perrone, D.: Global groundwater wells at risk of running dry, *Science*, 372, 418–421,  
691 <https://doi.org/10.1126/science.abc2755>, 2021.

692 Jie, F., Fei, L., Li, S., Hao, K., Liu, L., Li, J., and Liu, N.: Quantitative effects of vadose zone thickness on delayed recharge  
693 of groundwater for an irrigation district in an arid area of Northwest China, *J. Hydrol.: Reg. Stud.*, 40, 101022,  
694 <https://doi.org/10.1016/j.ejrh.2022.101022>, 2022.

695 Karandish, F., Liu, S. D., and De Graaf, I.: Global groundwater sustainability: a critical review of strategies and future  
696 pathways, *J. Hydrol.*, 657, 133060, <https://doi.org/10.1016/j.jhydrol.2025.133060>, 2025.

697 Kroes, J. G. and Supit, I.: Impact analysis of drought, water excess, and salinity on grass production in The Netherlands using  
698 historical and future climate data, *Agric. Ecosyst. Environ.*, 144, 370–381, <https://doi.org/10.1016/j.agee.2011.09.008>, 2011.

699 Kuang, X. X., Liu, J. G., Scanlon, B. R., Jiao, J. J., Jasechko, S., Lancia, M., Biskaborn, B. K., Wada, Y., Li, H. L., Zeng, Z.  
700 Z., Guo, Z. L., Yao, Y. Y., Gleeson, T., Nicot, J. P., Luo, X., Zou, Y. G., and Zheng, C. M.: The changing nature of groundwater  
701 in the global water cycle, *Science*, 383, <https://doi.org/10.1126/science.adf0630>, 2024.

702 Li, B. A., Sprenger, M., Wyatt, B. M., Giménez, D., Hirmas, D. R., Ajami, H., Wiekenkamp, I., Groh, J., Nimmo, J. R., Amato,  
703 M. T., Singh, N. K., Crompton, O., Araki, R., Xu, T. F., and Sullivan, P. L.: Ubiquity and causes of soil water preferential  
704 flow across 17 ecoregions. *Geophys. Res. Lett.*, 52, e2025GL118045, <https://doi.org/10.1029/2025GL118045>, 2025.

705 Li, Y. B., Liu, Y., Fan, H. Y., Xing, X. G., Wu, L., and Ma, X. Y.: Characteristics and simplified model of film slit irrigation,  
706 *Arch. Agron. Soil Sci.*, 65, 16–30, <https://doi.org/10.1080/03650340.2018.1477254>, 2018.

707 Liu, R. L., Zhong, B., Li, X. P., Zheng, K. Y., Liang, H., Cao, J. M., Yan, X., and Lyu, H. X.: Analysis of groundwater changes  
708 (2003–2020) in the North China Plain using geodetic measurements, *J. Hydrol.: Reg. Stud.*, 41, 101085,  
709 <https://doi.org/10.1016/j.ejrh.2022.101085>, 2022.

710 Long, D., Xu, Y. C., Cui, Y. J., Cui, Y. H., Butler, J. J., Dong, L., Wang, L. F., Liu, D. Y., Wada, Y., Hu, L. T., Bai, G. Y., Li,  
711 B. H., Wang, S. F., Nong, X. Z., Cai, Y., Cheng, C. S., Mu, Y. H., Qiao, Y., Wang, J. H., Wang, H., and Scanlon, B. R.:  
712 Unprecedented large-scale aquifer recovery through human intervention, *Nat. Commun.*, 16, 7296,  
713 <https://doi.org/10.1038/s41467-025-62719-5>, 2025.

714 Min, L. L., Shen, Y. J., and Pei, H. W.: Estimating groundwater recharge using deep vadose zone data under typical irrigated  
715 cropland in the piedmont region of the North China Plain, *J. Hydrol.*, 527, 305–315,  
716 <https://doi.org/10.1016/j.jhydrol.2015.04.064>, 2015.

717 Min, L. L., Qi, Y. Q., Shen, Y. J., Wang, P., Wang, S. Q., and Liu, M. Y.: Groundwater recharge under irrigated agro-  
718 ecosystems in the North China Plain: from a critical zone perspective, *J. Geogr. Sci.*, 29, 877–890,  
719 <https://doi.org/10.1007/s11442-019-1634-x>, 2019.

720 Moeck, C., Collenteur, R. A., Berghuijs, W. R., Luijendijk, E., and Gurdak, J. J.: A global assessment of groundwater recharge  
721 response to infiltration variability at monthly to decadal timescales, *Water Resour. Res.*, 60,  
722 <https://doi.org/10.1029/2023WR035828>, 2024.

723 Nan, T., Cao, W. G., Ren, Y. G., Sun, L., and Gao, Y. Y.: Evolution and influence factors of shallow groundwater depression  
724 cone in the Beijing–Tianjin–Hebei Plain, *South-to-North Water Transfers and Water Sci. Technol.* (in Chinese), 22, 110–121,  
725 <https://doi.org/10.13476/j.cnki.nsbdqk.2024.0013>, 2024.

726 Niswonger, R. G., Prudic, D. E., Pohl, G., and Constantz, J.: Incorporating seepage losses into the unsteady streamflow  
727 equations for simulating intermittent flow along mountain front streams, *Water Resour. Res.*, 41,  
728 <https://doi.org/10.1029/2004WR003677>, 2005.

729 O’Brien, R. M.: A Caution regarding rules of thumb for variance inflation factors. *Quality & quantity*, 41, 673–690,  
730 <https://doi.org/10.1007/s11135-006-9018-6>, 2007.

731 Oliver, M. A., and Webster, R.: A tutorial guide to geostatistics: Computing and modelling variograms and kriging, *Catena*,  
732 113, 56–69, <https://doi.org/10.1016/j.catena.2013.09.006>, 2014.

733 Pereira, L. S., Allen, R. G., Smith, M., and Raes, D.: Crop evapotranspiration estimation with FAO56: past and future, *Agric.*  
734 *Water Manag.*, 147, 4–20, <https://doi.org/10.1016/j.agwat.2014.07.031>, 2015.

735 Racz, A. J., Fisher, A. T., Schmidt, C. M., Lockwood, B. S., and Los Huertos, M.: Spatial and temporal infiltration dynamics  
736 during managed aquifer recharge, *Ground Water*, 50, 562–570, <https://doi.org/10.1111/j.1745-6584.2011.00875.x>, 2012.

737 Ruehl, C., Fisher, A. T., Hatch, C., Los Huertos, M., Stemler, G., and Shennan, C.: Differential gauging and tracer tests resolve  
738 seepage fluxes in a strongly losing stream, *J. Hydrol.*, 330, 235–248, <https://doi.org/10.1016/j.jhydrol.2006.03.025>, 2006.

739 Schübl, M., Brunetti, G., Fuchs, G., and Stumpp, C.: Estimating vadose zone water fluxes from soil water monitoring data: a  
740 comprehensive field study in Austria, *Hydrol. Earth Syst. Sci.*, 27, 1431–1455, <https://doi.org/10.5194/hess-27-1431-2023>,  
741 2023.

742 Scanlon, B. R., Fakhreddine, S., Rateb, A., De Graaf, I., Famiglietti, J., Gleeson, T., Grafton, R. Q., Jobbágy, E., Kebede, S.,  
743 Kolusu, S., Konikow, L. F., Long, D., Mekonnen, M., Schmied, H. M., Mukherjee, A., MacDonald, A., Reedy, R. C.,  
744 Shamsudduha, M., Simmons, C. T., Sun, A. L., Taylor, R. G., Villholth, K. G., Vörösmarty, C., and Zheng, C. M.: Global  
745 water resources and the role of groundwater in a resilient water future, *Nat. Rev. Earth Environ.*, 4, 87–101,  
746 <https://doi.org/10.1038/s43017-022-00378-6>, 2023.

747 Shanafield, M., Gutiérrez-Jurado, K., White, N., Hatch, M., and Keane, R.: Catchment-scale characterization of intermittent  
748 stream infiltration: a geophysics approach, *J. Geophys. Res.: Earth Surf.*, 125, e2019JF005330,  
749 <https://doi.org/10.1029/2019JF005330>, 2020.

750 Shirzaei, M., Freymueller, J., Törnqvist, T. E., Galloway, D. L., Dura, T., and Minderhoud, P. S. J.: Measuring, modelling,  
751 and projecting coastal land subsidence, *Nat. Rev. Earth Environ.*, 2, 40–58, <https://doi.org/10.1038/s43017-020-00115-x>, 2021.

752 Šimůnek, J., Brunetti, G., Jacques, D., Van Genuchten, M. T., and Sejna, M.: Developments and applications of the HYDRUS  
753 computer software packages since 2016, *Vadose Zone J.*, 23, <https://doi.org/10.1002/vzj2.20310>, 2024.

754 Šimůnek, J., Van Genuchten, M. T., and Sejna, M.: Hydrus: model use, calibration, and validation, *Trans. ASABE*, 55, 1261–  
755 1274, <https://doi.org/10.13031/2013.42239>, 2012.

756 Šimůnek, J., Van Genuchten, M. T., and Sejna, M.: Recent developments and applications of the HYDRUS computer software  
757 packages, *Vadose Zone J.*, 15, 1–25, <https://doi.org/10.2136/vzj2016.04.0033>, 2016.

758 Stafford, M. J., Holländer, H. M., and Dow, K.: Estimating groundwater recharge in the Assiniboine Delta Aquifer using  
759 HYDRUS-1D, *Agric. Water Manag.*, 267, 107514, <https://doi.org/10.1016/j.agwat.2022.107514>, 2022.

760 Szabó, B., Szatmári, G., Takács, K., Laborczi, A., Makó, A., Rajkai, K., and Pásztor, L.: Mapping soil hydraulic properties  
761 using random-forest-based pedotransfer functions and geostatistics, *Hydrol. Earth Syst. Sci.*, 23, 2615–2635,  
762 <https://doi.org/10.5194/hess-23-2615-2019>, 2019.

763 van Dam, J. C., Groenendijk, P., Hendriks, R. F. A., and Kroes, J. G.: Advances of modeling water flow in variably saturated  
764 soils with SWAP, *Vadose Zone J.*, 7, 640–653, <https://doi.org/10.2136/vzj2007.0060>, 2008.

765 van Genuchten, M. T.: A closed-form equation for predicting the hydraulic conductivity of unsaturated soils, *Soil Sci. Soc. Am.*  
766 *J.*, 44, 892–898, <https://doi.org/10.2136/sssaj1980.03615995004400050002x>, 1980.

767 Vereecken, H., Weihermüller, L., Assouline, S., Šimůnek, J., Verhoef, A., Herbst, M., Archer, N., Mohanty, B., Montzka, C.,  
768 Vanderborght, J., Balsamo, G., Bechtold, M., Boone, A., Chadburn, S., Cuntz, M., Decharme, B., Ducharne, A., Ek, M.,  
769 Garrigues, S., Goergen, K., Ingwersen, J., Kollet, S., Lawrence, D. M., Li, Q., Or, D., Swenson, S., De Vrese, P., Walko, R.,  
770 Wu, Y. H., and Xue, Y. K.: Infiltration from the pedon to global grid scales: an overview and outlook for land surface modeling,  
771 *Vadose Zone J.*, 18, 1–53, <https://doi.org/10.2136/vzj2018.10.0191>, 2019.

772 Vereecken, H., Weihermüller, L., Assouline, S., Šimůnek, J., Verhoef, A., Herbst, M., Archer, N., Mohanty, B., Montzka, C.,  
773 Vanderborght, J., Balsamo, G., Bechtold, M., Boone, A., Chadburn, S., Cuntz, M., Decharme, B., Ducharme, A., Ek, M.,  
774 Garrigues, S., Goergen, K., Ingwersen, J., Kollet, S., Lawrence, D. M., Li, Q., Or, D., Swenson, S., De Vrese, P., Walko, R.,  
775 Wu, Y. H., and Xue, Y. K.: Infiltration from the pedon to global grid scales: an overview and outlook for land surface modeling,  
776 *Vadose Zone J.*, 18, 1–53, <https://doi.org/10.2136/vzj2018.10.0191>, 2019.

777 Vogel, T., Van Genuchten, M. T., and Cislérova, M.: Effect of the shape of the soil hydraulic functions near saturation on  
778 variably saturated flow predictions, *Adv. Water Resour.*, 24, 133–144, [https://doi.org/10.1016/S0309-1708\(00\)00037-3](https://doi.org/10.1016/S0309-1708(00)00037-3), 2001.

779 Wang, W. Z., Xia, Y., Sun, J. N., Liu, Y. Z., Li, P. Y., Han, F. P., and Li, Z.: Uncertainties in physical and tracer methods in  
780 actual groundwater recharge estimation in the thick loess deposits of China, *J. Hydrol.*, 634, 131127,  
781 <https://doi.org/10.1016/j.jhydrol.2024.131127>, 2024.

782 Wang, X. S., Ma, M. G., Li, X., Zhao, J., Dong, P., and Zhou, J.: Groundwater response to leakage of surface water through a  
783 thick vadose zone in the middle reaches area of Heihe River Basin, China, *Hydrol. Earth Syst. Sci.*, 14, 639–650,  
784 <https://doi.org/10.5194/hess-14-639-2010>, 2010.

785 Weihermüller, L., Lehmann, P., Herbst, M., Rahmati, M., Verhoef, A., Or, D., Jacques, D., and Vereecken, H.: Choice of  
786 pedotransfer functions matters when simulating soil water balance fluxes, *J. Adv. Model. Earth Syst.*, 13,  
787 <https://doi.org/10.1029/2020MS002404>, 2021.

788 Wesseling, J. G. and Feddes, R. A.: Assessing crop water productivity from field to regional scale, *Agric. Water Manag.*, 86,  
789 30–39, <https://doi.org/10.1016/j.agwat.2006.06.011>, 2006.

790 Wolf, C., Gurdak, J. J., Lauffenburger, Z., Nanus, L., and Maurer, E.: Controls on recharge in thick vadose zones under climate  
791 variability and change, *Hydrogeol. J.*, 30, 1637–1655, <https://doi.org/10.1007/s10040-022-02504-6>, 2022.

792 Wu, L., Min, L. L., Liu, M. Y., Zhang, Y. C., Pei, H. W., Li, H. J., Zhang, G. L., Wang, S. Q., and Shen, Y. J.: Monitoring of  
793 thick vadose zone water dynamics under irrigation using a 48 m deep caisson at the Luancheng Critical Zone Observatory,  
794 *Water Resour. Res.*, 59, <https://doi.org/10.1029/2022WR032965>, 2023.

795 Xi, H. Y., Zhang, L., Feng, Q., Si, J. H., Chang, Z. Q., and Yu, T.: The spatial heterogeneity of riverbed saturated permeability  
796 coefficient in the lower reaches of the Heihe River Basin, Northwest China, *Hydrol. Process.*, 29, 4891–4907,  
797 <https://doi.org/10.1002/hyp.10544>, 2015.

798 Yin, X. R., Shu, L. C., Wang, Z., Li, Y. X., Zhou, L., Lv, C., Li, S., Liu, B., and Lu, C. P.: Quantifying the time-varying period  
799 and time lag features of groundwater response: dynamic impacts of precipitation-fed groundwater recharge, *Ecol. Indic.*, 176,  
800 113648, <https://doi.org/10.1016/j.ecolind.2025.113648>, 2025.

801 Zafarmomen, N., Alizadeh, H., Bayat, M., Ehtiat, M., and Moradkhani, H.: Assimilation of Sentinel-based leaf area index for  
802 modeling surface–ground water interactions in irrigation districts, *Water Resour. Res.*, 60, e2023WR036080,  
803 <https://doi.org/10.1029/2023WR036080>, 2024. Zhang, Y. G. and Schaap, M. G.: Weighted recalibration of the Rosetta  
804 pedotransfer model with improved estimates of hydraulic parameter distributions and summary statistics (Rosetta3), *J. Hydrol.*,  
805 547, 39–53, <https://doi.org/10.1016/j.jhydrol.2017.01.004>, 2017.

806 Zhang, Y. J., Yuan, J. G., and Zhang, S.: Spatial–temporal change of leaf area index (LAI) of vegetation in Hebei Province  
807 from 2002 to 2011, *J. Nanjing For. Univ. (Nat. Sci. Ed.)* (in Chinese), 39, 86–92, <https://doi.org/10.3969/j.issn.1000-2006.2015.01.016>, 2015.

809 Zhao, W., Jia, X. Y., Wu, L. S., Liu, P., and Zhang, H.: Analysis of influencing factors of groundwater level change in  
810 Ningbailong groundwater funnel, *Water Resour. Plan. Des.* (in Chinese), 11, 48–52, <https://doi.org/10.1672-2469.2020.11.013>,  
811 2020.

812 Zhou, H., Dai, M., Wei, M., and Luo, Z. C.: Quantitative assessment of shallow groundwater sustainability in North China  
813 Plain, *Remote Sens.*, 15, 474, <https://doi.org/10.3390/rs15020474>, 2023.